processes

MDPI

Article

Theranostic Iron Oxide Nanoparticles for Controlled Oxaliplatin Release Under Simulated Circulation and Cytotoxicity Evaluation in Colorectal Cancer Cell Lines

Masome Moeni [1], Mohamed Edokali [1], Alistair Bacchetti [2], Joshua Davy [2], Hanyang Sun [3], Matthew Rogers [4], Oscar Cespedes [4], Zabeada Aslam [1], Andrew Britton [1], Leah Khazin [5], Jurgen E. Schneider [5], Pietro Valdastri [2], Robert Menzel [6], Milene Volpato [3] and Ali Hassanpour [1,*]

[1] School of Chemical and Process Engineering, Faculty of Engineering and Physical Science, University of Leeds, Leeds LS2 9JT, UK; masomemoeni@yahoo.com (M.M.)
[2] Science and Technologies of Robotics in Medicine (STORM) Lab, School of Electronic and Electrical Engineering, University of Leeds, Leeds LS2 9JT, UK
[3] Leeds Institute of Medical Research, St James University Hospital, University of Leeds, Leeds LS9 7TF, UK; umhsu@leeds.ac.uk (H.S.)
[4] School of Physics and Astronomy, Faculty of Engineering and Physical Science, University of Leeds, Leeds LS2 9JT, UK
[5] Leeds Institute of Cardiovascular and Metabolic Medicine, University of Leeds, Leeds LS2 9JT, UK
[6] School of Chemistry, Faculty of Engineering and Physical Science, University of Leeds, Leeds LS2 9JT, UK
* Correspondence: a.hassanpour@leeds.ac.uk; Tel.: +44-(0)-113-343-2405

Abstract

Oxaliplatin (OXA) is a chemotherapeutic agent that suffers from poor pharmacokinetics and off-target toxicity. To enable controlled OXA release, we engineered a multi-functional iron oxide nanoparticle (IONPs) drug delivery system, based on pH-responsive mesoporous Fe_3O_4 (Fe_3O_4@MSN-NH_2) nanoparticles (NPs), conjugated with folic acid (FA) for receptor-mediated targeting and guided by a magnetic robot platform (MRP) under simulated physiologically relevant dynamic circulation/flow system. For FA-conjugated NPs (Fe_3O_4@MSN-NH_2/FA), ~29.73% OXA loading was achieved compared to ~10.3% in controls (Fe_3O_4@MSN-NH_2/OXA), quantified by ICP-OES. Under dynamic circulation flow over 48 h, MRP enhanced pH-responsive OXA release (quantified by HPLC-UV), reaching ~92% and 88% (Fe_3O_4@MSN-NH_2/OXA and Fe_3O_4@MSN-NH_2/FA, respectively) at pH 5, versus 47% and 40% (Fe_3O_4@MSN-NH_2/OXA and Fe_3O_4@MSN-NH_2/FA, respectively) without MRP, demonstrating precise control in acidic tumor-mimicking conditions. MRI relaxometry exhibited strong T2-weighted contrast (T2 = 0.015 s at 50 µg/mL for Fe_3O_4@MSN-NH_2/FA/OXA), confirming theranostic potential. Reverse transcription quantitative polymerase chain reaction (RT-qPCR) studies revealed variable Folate receptor alpha (FOLR1) expression among colorectal cancer cell lines (Caco2, SW620, SW48, and T84), with Caco2 demonstrating high levels. MTT assays indicated selective targeting of FOLR1-positive cells by FA-functionalized NPs (Fe_3O_4@MSN-NH_2/FA). This multi-functional drug delivery system integrates targeted delivery, MRP release, and real-time imaging, offering a promising technique for precision oncology.

Keywords: oxaliplatin; multi-functional; iron oxide nanoparticles; folic acid; theranostic; magnetic robot platform; colorectal cancer cells

Check for updates

Received: 14 November 2025
Revised: 23 January 2026
Accepted: 2 February 2026
Published: 9 February 2026

Copyright: © 2026 by the authors. Licensee MDPI, Basel, Switzerland. This article is an open access article distributed under the terms and conditions of the Creative Commons Attribution (CC BY) license.

1. Introduction

Chemotherapy remains a cornerstone in cancer therapy, with agents such as doxorubicin (DOX), docetaxel, paclitaxel, cisplatin, carboplatin, and oxaliplatin (OXA) improving survival rates [1,2]. OXA is commonly employed in the treatment of gastrointestinal cancers, where it induces immunogenic cell death and is used in both adjuvant and palliative settings [3–6]. However, its clinical utility is restricted by poor pharmacokinetics and adverse off-target toxicity, including acute neurotoxicity caused by accumulation of platinum (Pt) in spinal ganglion cells, damaging the cell body and axon [7–9]. Systemic chemotherapy fails to differentiate between malignant and healthy cells [10], leading to poor prognosis, undesirable side effects, drug resistance, and cancer recurrence [11,12].

To overcome these challenges, targeted drug delivery (TDD) systems have gained attention, aiming to improve drug circulation, increase accumulation in the tumor microenvironment (TME), enhance tissue penetration and cellular uptake, and facilitate controlled drug release (CDR) [13]. Recent developments in nanomedicine have explored tumor-responsive and stimuli-responsive nanoplatforms to improve the therapeutic efficacy and reduce adverse systemic reactions [14–16].

Within this evolving field of smart nanomedicines, iron oxide nanoparticles (IONPs) stand out due to their unique magnetic and imaging functionalities. Specifically, magnetite (Fe_3O_4) NPs provide promising features for TDD, because of their biocompatibility, magnetic susceptibility [17–19], and their established role as contrast agents for magnetic resonance imaging (MRI) in theranostic platforms that facilitate simultaneous imaging and therapy [20]. They can penetrate anatomical barriers, for instance, the blood–brain barrier, depending on their surface functionalization (e.g., lactoferrin and transferrin ligands) [21]. Drug delivery via IONPs can be achieved via passive targeting depending on NP properties (size, shape, charge and polarity) or active targeting, which involves ligand–receptor interactions [22–25]. Receptor–ligand interactions are vital in the active targeting of nano-agents [26], involving for instance epidermal growth factor receptors [27], folate receptors (FRs) [28], G protein-coupled receptors [29,30], and fibroblast growth factor receptors [31]. Folate receptor alpha (FOLR1), a glycoprotein with high folate affinity, is highly overexpressed in many carcinomas to support the rapid proliferation of cancer cells [32]. Folic acid, the synthetic form of folate (vitamin B9) [33,34], is widely applied to functionalize IONPs for receptor-mediated uptake and CDR [35–37]. In colorectal cancer, FOLR1 expression differs across cell lines such as Caco2, SW620, T84, and SW48, making them appropriate models for studying receptor-mediated targeting [38].

Uncoated Fe_3O_4 NPs face several limitations including aggregation due to high surface energy, susceptibility to oxidation which compromises dispersity and magnetization, and a high chemical reactivity that leads to undesirable interactions [39–41]. These drawbacks can be mitigated by surface coating to optimize therapeutics performance both in vitro and in vivo [17,42,43]. Silica (SiO_2) coating can improve dispersibility and enhance drug loading [44–47], while functionalization with amine groups (-NH_2) facilitates drug attachment and improves circulation time [48]. However, Fe_3O_4 NPs functionalized with SiO_2-NH_2 groups rely on passive targeting for delivery [49–54]. Feng et al. [51] demonstrated that Fe_3O_4 NPs functionalized with mesoporous silica NPs (MSNs) and NH_2 groups (Fe_3O_4@MSN-NH_2) and modified with hyaluronic acid enabled active DOX targeting to 4T1 breast cancer cells, improving therapeutic efficacy [51]. In addition to conventional chemical surface functionalization strategies, emerging eco-friendly (green) synthesis pathways provide an alternative method to functionalize NPs directly [55].

Magnetic robot platforms (MRPs) enable wireless navigation of ferromagnetic bodies, including Fe_3O_4 NPs, with high spatial precision and have received significant attention for TDD and CDR in dynamic biomedical environments [56–58]. A common configuration

involves an electro-permanent magnetic (EPM) platform, which uses an industrial robotic arm equipped with a permanent magnet end-effector. Adjusting the robot's joints and end-effector position allows optimal EPM positioning for targeted actuation [59]. Although this approach is a promising technique, the integration of MRP for NP navigation and pH-responsive drug release under a simulated in vivo dynamic circulation system remains underexplored. For this purpose, the magnetic responsiveness of NPs is a critical property for MRP applications; however, maintaining it after surface coating and drug loading remains a major challenge [53,54].

Recent studies have investigated Fe_3O_4@MSN-NH_2-based nanocarriers for pH-responsive drug release under static conditions. Notably, Tabasi et al. [53] developed pH-responsive Fe_3O_4@MSN-NH_2/OXA NPs with enhanced OXA loading [53]. The results were promising for the cancer cell lines; however, the release study was conducted under static conditions, which do not adequately represent the dynamic forces that govern NP stability and diffusion behavior in vivo. To the best of our knowledge, no studies have investigated the MRP-controlled release profile of OXA from FA-conjugated Fe_3O_4 NPs under a simulated dynamic circulation/flow system.

This study addresses key shortcomings by utilizing Fe_3O_4@MSN-NH_2-based nanocarriers, conjugating FA targeting ligands and implementing MRP-assisted drug release under continuous circulation. Furthermore, our formulations address issues related to temperature-dependent stability (storage, room, human body, and hyperthermia temperatures), aggregation during functionalization, OXA loading, and release feasibility under MRP actuation. Comprehensive analytical methods were conducted to substantiate functionalization, quantify OXA loading, and validate performance. Gene expression analysis using reverse transcription quantitative polymerase chain reaction (RT-qPCR) was performed to quantify relative folate receptor alpha (FOLR1) levels across different cell lines, providing insights into potential targeting strategies. Additionally, the MTT assay was conducted to investigate cell viability following exposure to nanoparticle formulations and oxaliplatin, enabling a comparative assessment of therapeutic efficacy and biocompatibility. Our study offers a substantial step forward compared to previously reported TDD systems.

2. Materials and Methods

2.1. Chemicals and Materials

Anhydrous iron (III) chloride ($FeCl_3$, AR grade), iron (II) sulfate heptahydrate ($FeSO_4 \cdot 7H_2O$, AR grade), cetyltrimethylammonium bromide (CTAB, $\geq$96.0%), tetraethyl orthosilicate (TEOS, 98%), 3-aminopropyltriethoxysilane (APTES), N-hydroxysuccinimide (NHS, 98%), ammonium nitrate (NH_4NO_3), phosphate-buffered solution (PBS), dimethyl sulfoxide (DMSO), and cellulose dialysis tubing (D9722, 10.0 mm flat width) were obtained from Sigma Aldrich (Dorset, UK). 1-ethyl-3-(3-dimethylaminopropyl) carbodiimide (EDCI), N-Methyl-2-pyrrolidone (NMP, 99%), acetate buffer (AcB), and 3-(4,5-dimethylthiazol-2-yl)-2,5-diphenyltetrazolium bromide (MTT) (M6494) were acquired from Thermo Fisher Scientific (Birmingham, UK). Ethanol (EtOH) absolute (AR grade, $\geq$99.8%) and high-performance liquid chromatography grade water (HPLCW) were supplied by VWR International Chemicals (Lutterworth, UK). Ammonium hydroxide (NH_4OH 25–30 wt.% in water, AR grade) was purchased from Merck Life Science UK Limited (Dorset, UK)and OXA was obtained from Molekula Group (Darlington, UK). Folic acid (FA) was purchased from Cayman Chemical Company. RPMI-1640 medium was supplied by Scientistic Laboratory Supplies (Nottingham, UK). Fetal calf serum (FCS) and trypsin were obtained from Fisher Scientific Ltd. (Loughborough, UK) Caco2, SW620, T84, and SW48 human colorectal cancer cell lines were obtained from the American Type Culture Collection (ATCC, Manassas, VA, USA) and authenticated by short tandem repeat (STR) profiling prior to use.

2.2. Preparation of Mesoporous Fe_3O_4@MSN-NH_2 Nanoparticles

A detailed overview of chemicals, quantities, experimental conditions, and post-reaction rinsing stages used throughout the synthesis of nanoparticles is available in Supplementary Information Section, Table S1.

Fe_3O_4 NPs were prepared via the co-precipitation method as outlined in our earlier study [60]. Briefly, the precursors, $FeCl_3$ and $FeSO_4 \cdot 7H_2O$, were dispersed in HPLCW and EtOH under N_2 flow and stirred for 45 min at 80 °C. The pH was adjusted to 11 by NH_4OH and the reaction was stopped with no aging. The synthesized Fe_3O_4 NPs were kept in a wet paste form (50% *w*/*w*) (WET). The synthesis of Fe_3O_4@MSN-NH_2 was adapted from our recent publication [61]. The WET Fe_3O_4 NPs (1.0 g 50% *w*/*w*) were suspended in HPLCW (120.0 mL) and EtOH (60.0 mL), and the solution was sonicated in an ice bath for 45 min. NH_4OH (1.2 mL) was added dropwise under an inert environment and stirred for 1 h at room temperature. Following the dropwise addition of CTAB (0.0729 g) into the solution, TEOS (1.3 mL) was introduced gradually in a controlled manner, and the reaction was left to proceed at ambient conditions for 24 h. The product (Fe_3O_4@CTAB-SiO_2) was rinsed with EtOH and HPLCW multiple times and collected through centrifugation (10,000 rpm, 45 min, 25 °C) and a permanent magnet. A total of 0.560 g (50% *w*/*w*) of the WET Fe_3O_4@CTAB-SiO_2 was dispersed in EtOH (50.0 mL), followed by controlled addition of APTES (1.2 mL) while stirring (400 rpm) under N_2 flow at room temperature for 24 h. The resulting product (Fe_3O_4@CTAB-SiO_2-NH_2) underwent several washes with EtOH and was separated by a centrifuge and a permanent magnet. The WET Fe_3O_4@CTAB-SiO_2-NH_2 (0.560 g, 50% *w*/*w*) was suspended in EtOH (60.0 mL) and sonicated in an ice bath for 45 min. Separately, NH_4NO_3 (0.006 g/mL, 0.240 g) was dissolved in HPLCW (10 mL) (Supplementary Information Equation (S1)), then it was slowly added to the solution and refluxed for 12 h at 60 °C to remove the CTAB. The reflux temperature of 60 °C was chosen to enable complete removal of CTAB without the compromising the magnetic integrity of the Fe_3O_4 core, based on our previous optimization study [61].

The product (Fe_3O_4@MSN-NH_2) was first washed with HPLCW to remove the surface-bound NH_4^+ ions and the remaining NO_3^-; then, EtOH was used to rinse away the CTAB (Equation (2)). The NPs were recovered by centrifugation and a permanent magnet.

2.3. Preparation of Fe_3O_4@MSN-NH_2/FA in the Dark

A total of 0.086 g of EDCI and 0.077 g of NHS were dissolved in 23.0 mL NMP, purged with N_2 gas, and stirred for 1 h. Then, 0.050 g of folic acid was gradually added to the solution, and the reaction was conducted in the dark at room temperature for 24 h. In a separate flask, the Fe_3O_4@MSN-NH_2 (0.560 g, 50% *w*/*w*) NPs were dispersed in NMP (85.0 mL) and sonicated, then kept stirred under inert environment and room temperature. The activated folic acid was introduced dropwise to the NP solution and stirred under the same conditions for 48 h. The product (Fe_3O_4@MSN-NH_2/FA) was initially rinsed with EtOH followed by HPLCW and separated by centrifuge and the permanent magnet.

2.4. Drug Loading (Fe_3O_4@MSN-NH_2/OXA and Fe_3O_4@MSN-NH_2/FA/OXA)

The WET Fe_3O_4@MSN-NH_2 (0.560 g, 50% *w*/*w*) or Fe_3O_4@MSN-NH_2/FA (0.560 g, 50% *w*/*w*) was re-dispersed in HPLCW (10.0 mL) and sonicated in an ice bath for 45 min. For each sample, OXA (0.005 g/mL) was separately dissolved in 7.24 mL EtOH and sonicated for 5 min at 45 °C under dark conditions. The OXA solution was added dropwise to each NP solution and stirred (300 rpm) in the dark, under N_2 flow at ambient temperature for 48 h (see Figure 1). The products (Fe_3O_4@MSN-NH_2@OXA and Fe_3O_4@MSN-NH_2/FA/OXA) were rinsed with EtOH and HPLCW and recovered by centrifugation and a permanent magnet. The loading capacity of OXA was investigated by ICP-OES instrument.

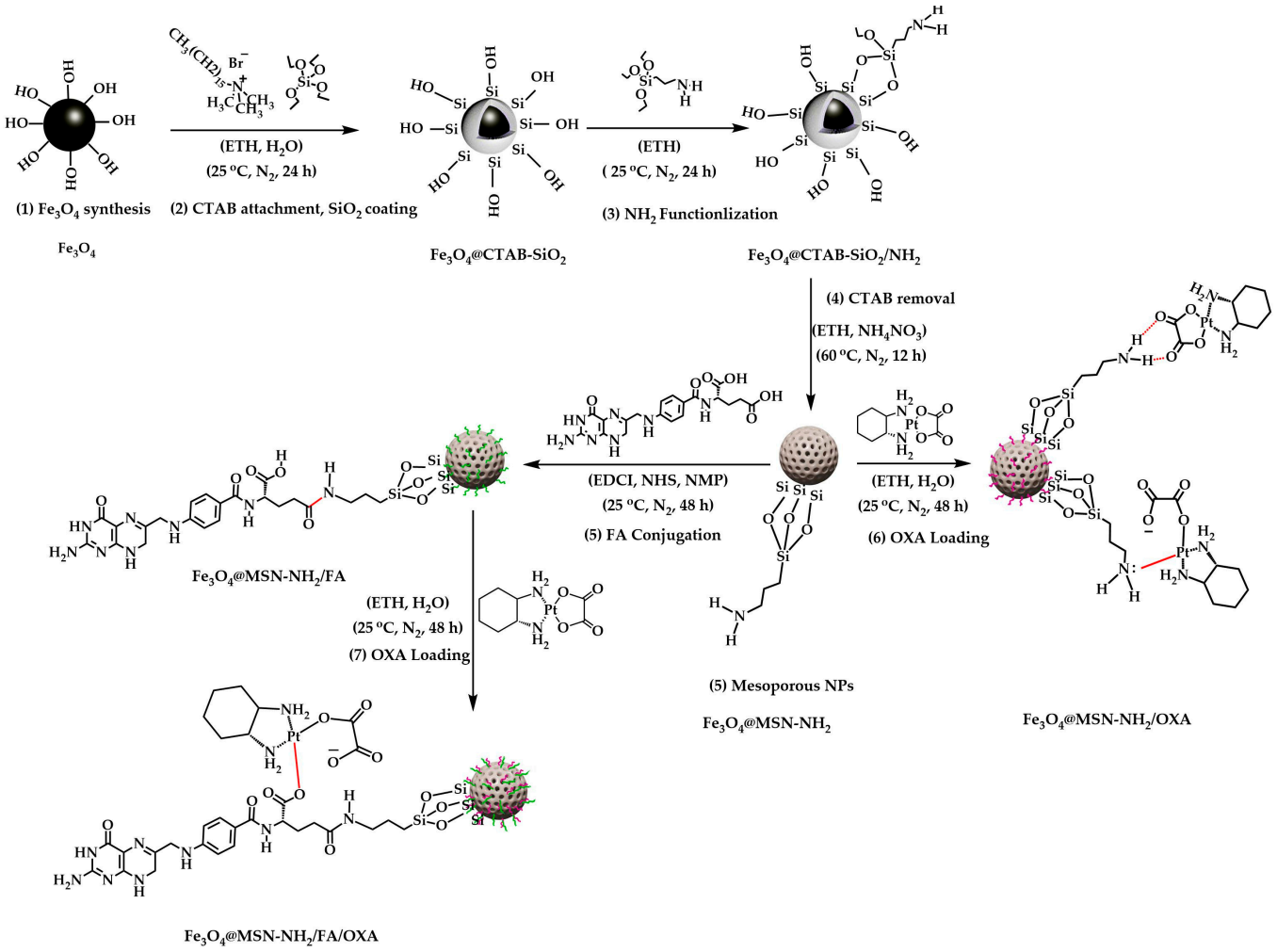

Figure 1. Stepwise schematic of Fe_3O_4 NP synthesis, CTAB attachment, SiO_2 coating, NH_2 functionalization, CTAB removal, mesoporous NPs, conjugation of FA, and OXA loading.

2.5. External Magnetic Robot-Assisted Localized Release of Oxaliplatin

A closed-loop dynamic perfusion system was developed to simulate in vivo-like circulation and study OXA release from Fe_3O_4@MSN-NH_2/OXA and Fe_3O_4@MSN-NH_2/FA/OXA. In this setup, the NP colloidal suspension continuously recirculated from the reservoir through the pump and into two tissue-mimicking chambers (Chamber 1: tumor mimicking, pH 5.0; Chamber 2: physiological condition, pH 7.4) with and without the MRP assistance for site-specific accumulation and release. In the MRP system, as displayed in Figure 2, a peristaltic pump (Fisher Scientific, Waltham, MA, USA) was connected to a PBS (pH 7.4) reservoir containing 10.0 mL (0.5 mg/mL) of the OXA-loaded samples, suspended in 100.0 mL PBS. The reservoir was placed on a magnetic stirrer plate, operating at a constant temperature of 37 °C and stirring rate of 460 rpm. A controlled flow rate of ~4.0 mL s^{-1} was selected based on the pump's preset options and physiological values found in vessels supplying cerebral regions [62] to simulate unidirectional flow through tissue-mimicking environments.

Each environment was localized within a single 3D-printed chamber, housing a tubular cellulose membrane with a cross-sectional diameter of 7 mm under the specified flow conditions. Chamber 1 contained 20.0 mL of acetate buffer (pH 5.0) to simulate an acidic TME. Chamber 2 contained 20.0 mL of PBS (pH 7.4) to represent healthy tissue. A robotic arm (IIWA 14, KUKA, Shelby Township, MI, USA) equipped with an EPM end-effector (neodymium–iron–boron, N52 grade, 1.48 T) was placed at approximately

150.0 mm above Chamber 1 to investigate magnetically guided drug diffusion into acidic tumor conditions as shown in Figure 2 and Video S1. In this setup, the MRP magnetically guided and accumulated NPs within the tumor-mimicking acidic chamber, while simultaneously facilitating localized, pH-responsive OXA release by increasing NP retention and diffusion. Samples (1 mL in volume) were extracted from each chamber at 1, 3, 6, 9, 12, 24, 30, and 48 h intervals. The amount of OXA released under MRP guidance was quantified using high-performance liquid chromatography with ultraviolet detection (HPLC-UV, Agilent Technologies, Santa Clara, CA, USA). The navigation of Fe_3O_4@MSN-NH_2/OXA by MRP is also visualized in Video S2. A summary of the information for the magnetic robot platform (MRP) setup and the dynamic circulation/flow system parameters is provided in Table S2.

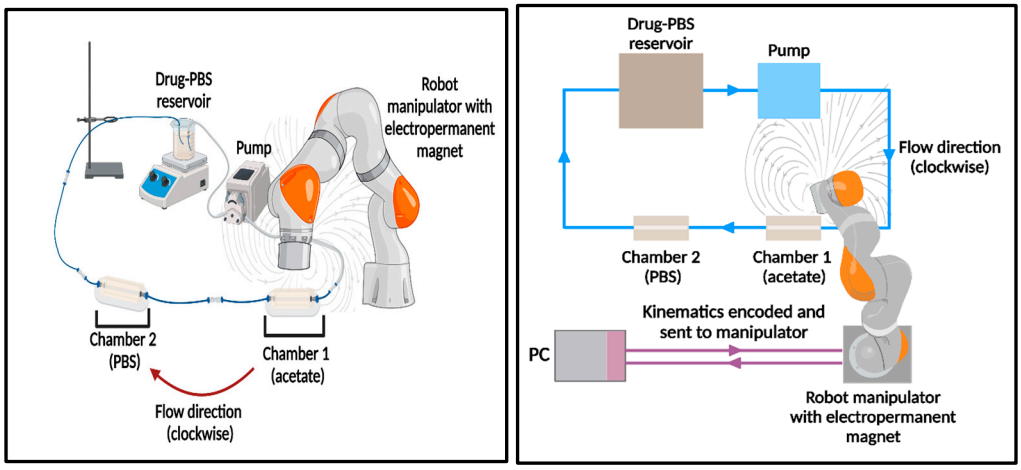

(**a**) (**b**)

Figure 2. Schematic of the experimental setup and localized magnetic drug guidance under simulated in vivo-like dynamic flow (MRP-assisted system). (**a**) Experimental configuration displaying clockwise flow from a reservoir (PBS, 100.0 mL) containing OXA (10.0 mL) samples, directed by a peristaltic pump (flow rate: 4.0 mL s^{-1}) through a simulated tumor chamber (Chamber 1, AcB 20 mL, pH 5.0) and a healthy tissue chamber (Chamber 2, PBS 20 mL, pH 7.4). (**b**) Simplified schematic illustrating flow direction, component layout, and robotic manipulator connections for external magnetic robot-assisted OXA release.

2.6. Characterizations

The functionalization of Fe_3O_4 nanoparticles was characterized using a Bruker Vertex 80V FT-IR spectrometer (Bruker Optik GmbH, Ettlingen, Germany), equipped with an RT-DLaTGS detector and a Bruker A225/Q Platinum single-bounce ATR accessory (Bruker Optik GmbH, Ettlingen, Germany) with a diamond crystal. Measurements were performed in the 4000–600 cm^{-1} range, with a resolution of 4 cm^{-1} and 32 scans using the attenuated total reflection (ATR) technique. The structural and crystalline phases of the nanoparticles were characterized using a Bruker D2 Phaser powder X-ray diffractometer (PXRD) (Bruker AXS GmbH, Karlsruhe, Germany) equipped with Cu-Kα radiation (λ = 1.541 Å) and a LinxEye detector, operating at 40 kV and 40 mA. Scans were performed over an angular range of $5° \leq 2\theta \leq 80°$, with an exposure time of 10 s per step and a total measurement duration of 11 h. Surface morphology and elemental composition of the nanoparticles were examined using an FEI Tecnai TF20 TEM (FEI Company, Hillsboro, OR, USA) equipped with a field emission gun (FEG), a HAADF detector, an Oxford Instruments INCA 350 EDX (Oxford Instruments, Abingdon, UK) system with an 80 mm X-Max SDD detector (Gatan Inc., Pleasanton, CA, USA), and a Gatan Orius SC600A CCD camera (Gatan Inc., Pleasanton, CA, USA). Dynamic light

scattering (DLS) was used to determine the hydrodynamic size (DH), and zeta potential (ZP) was measured to assess the particle charge of the nanoparticles (NPs) in the solution using a Zetasizer (Nano ZSP ZE5600, Malvern Panalytical Ltd., Malvern, UK). For the analysis, the samples were dispersed in HPLCW and homogenized using a Fisher Scientific™ FB705 (Fisher Scientific, Waltham, MA, USA) sonic dismembrator ultra-sonic probe at 30% amplitude with a power output of approximately 210, delivering 2000 J energy over 2 min in continuous mode, while keeping the sample in an ice bath to prevent overheating. The samples were then dispensed in a disposable cuvette and analyzed. The stability of nanoparticle dispersions in PBS was assessed using a Dispersion Analyzer (LUMiSizer 6112-29, 12-channel, ADAPTIVE INSTRUMENTS, LUM GmbH, Berlin, Germany) operating at a wavelength of 865 nm, with light factors ranging from 0.25 to 6. Thermal stability and degradation profiles of the NPs were analyzed by thermogravimetric analysis (TGA) and differential scanning calorimetry (TGA/DSC). The analyses were carried out on Mettler Toledo TGA/DSC 3 + instrument (Mettler-Toledo (Schweitz) GmbH, Greifensee Zurich, Switzerland) between 30 and 700 °C at a heating rate of 5 °C min^{-1} under N_2 gas. Derivative thermogravimetry (DTG) curves were applied to determine the temperature of maximum weight loss for the NP components. The magnetic properties of the dried nanoparticles were analyzed using a superconducting quantum interference device vibrating sample magnetometer (SQUID-VSM, Quantum Design Inc., San Diego, CA, USA) at 300 K under a magnetic field of 7 T. The platinum content in the samples was quantified by inductively coupled plasma optical emission spectrometry (ICP-OES, Thermo Scientific iCAP7400 radial, Waltham, MA, USA) equipped with a Cetac ASX-520 autosampler (Teledyne CETA, Omaha, NE, USA), the Thermo Qtegra software (Version 2.6, Agilent Technologies), a quartz Seaspray nebuliser, and a quartz cyclonic spray chamber. OXA was quantified using HPLC-UV (Agilent Technologies, Santa Clara, CA, USA) on an Agilent 1290 Infinity II system (Agilent, Santa Clara, CA, USA) equipped with a diode array detector (DAD) set at 254 nm. Chromatographic separation was performed on an Agilent InfinityLab Poroshell 120 EC-C18 column (2.1 × 50 mm, 1.9 µm, Agilent Technologies, Santa Clara, CA, USA) maintained at 40 °C. The mobile phase consisted of 0.1% trifluoroacetic acid (TFA) in water (95%) and 0.1% TFA in acetonitrile (5%). Gradient elution was started with 5% water and was sustained for 5 min at a constant flow rate of 0.5 mL/min. The elemental composition and chemical states of the nanoparticles were analyzed using an ultra-high vacuum (UHV) X-ray photoelectron spectroscopy (XPS) system equipped with an SPECS Phoibos 150 (SPECS Surface Nano Analysis GmbH, Berlin, Germany) hemi-spherical analyzer and 1D-DLD detectors. The X-ray source was a monochromated Al Kα line with a photon energy of 1486.7 eV, operating at 400 W and 15 kV. The vacuum is approximately at 1×10^{-9} mbar. During the measurements, an electron flood gun is applied to charge neutralize NPs. The dried powder NPs were pressed onto the tape attached to an omicron sample plate. Binding energy was calibrated to the adventitious carbon peak at 284.8 eV. The surface area and porosity of the dried nanoparticle powders were determined using a Brunauer–Emmett–Teller (BET) adsorption–desorption analyzer (Nova 800 series, Anton Paar GmbH, Graz, Austria) operated with Anton Paar Kaomi software (Version 2.0). Relaxometry measurements were performed using a Bruker BioSpec 70/20 USR 7 Tesla preclinical MRI scanner (Bruker BioSpin, Ettlingen, Germany), equipped with a 660 mT/m gradient and a four-element volume array coil (Neos BioTec, Pamplona, Spain). T1 relaxation times were measured using an Inversion Recovery (IR) spin echo (SE) sequence, with the following parameters: echo time (TE) = 4.49 ms, repetition time (TR) = 15,000 ms, matrix size = 128 × 128, field of view (FOV) = 35 × 35 mm, axial slice thickness = 1 mm, and 22 inversion times, varied between 0.00687 s and 7.5 s. T2

mapping was carried out using a multi-echo SE sequence with the same parameters, but comprising 64 echoes without inversion pulse and a TR = 5 s. Relaxation maps were generated using in-house-developed software and region-of-interest (ROI) analysis across phantom samples. Phantoms were prepared by dispersing the NPs at concentrations of 50 μg/mL and 5 μg/mL in Milli-Q water and sonicating in an ice bath for 45 min. Each dispersion was mixed in 1:1 ratio with 1% agarose solution (prepared at 70–80 °C) and transferred into 1 mL syringes to solidify. Syringes were placed in a bespoke 3D-printed sample holder and inserted in the radiofrequency (RF) coil of the MRI system.

2.7. FOLR1 Gene Expression Analysis

Human colorectal cancer cell lines (Caco2, SW620, T84 and SW48 cells) were grown to 70% confluence in the RPMI medium, with 10% (*v*/*v*) heat-inactivated FCS. Total RNA was extracted (New England Biolabs, T2010S, Ipswich, MA, USA). cDNA was synthesized from 500 ng RNA using the LunaScript RT SuperMix Kit (New England Biolabs, E3010, Ipswich, MA, USA). Both steps were performed according to the manufacturer's instructions. Luna Universal qPCR Master Mix kit (New England Biolabs, M3003S, Ipswich, MA, USA) was used for Reverse Transcription Quantitative Polymerase Chain Reaction (RT-qPCR), according to the manufacturer's instructions, using 1 uL cDNA input. Each reaction was carried out with 1 μL of cDNA input using the QuantStudio 5 Real-Time PCR System (Thermo Fisher Scientific, Waltham, MA, USA). The primers used were FOLR1 forward: AGCACCACAAGGAAAAGCCAGG; FOLR1 reverse: GTGCCATCTCTC-CACAGTGGTT; GAPDH forward: TCAACGACCACTTTGTCAAGC; GAPDH reverse: CCAGGGTCTTACTCCTTGG. Relative quantification was obtained using the 2 ($^{-\Delta\Delta Ct}$) method. Expression values were calculated as $\log_2$ fold-change relative to the T84 cells as the reference for $^{\Delta\Delta Ct}$ normalization.

2.8. MTT Cytotoxicity Assay

Caco2 and SW48 cells were seeded into 96-well plates at a density of 1000 cells per well in an RPMI medium supplemented with 10% (*v*/*v*) heat-inactivated FCS and incubated at 37 °C in a humidified atmosphere containing 5% CO_2. After 24 h incubation, NP formulations and pure OXA were dispersed in culture medium (0.5 mg/mL). The NPs were sonicated for 45 min in an ice bath, while pure OXA was sonicated for 15 min at 45 °C. Serial dilutions of either pure OXA or NP suspensions were then prepared in culture medium. The cells were exposed to either a carrier control or drug/particle concentrations for 72 h. MTT solution (5 mg/mL in PBS) was then added (20 μL/well) to each well and incubated for 4 h. The media were removed, and 150 μL of DMSO was added to dissolve formazan crystals. Once the crystals fully were fully dissolved, absorbance was measured at 620 nm using Cytation^{TM} 5 Imaging Multimode Reader (BioTek, Winoosi, VT, USA). Statistical analysis was conducted in Prism 9, using the two-way ANOVA test with Geisser–Greenhouse correction. IC_{50} values were calculated using non-linear regression analysis (log(inhibitor) vs. normalized response, variable slope) in GraphPad Prism (Version 10.0.0, GraphPad Software, Boston, MA, USA), with cell growth normalized to the carrier control.

3. Results and Discussion

Fe_3O_4 NPs were synthesized into mesoporous carriers with amine groups and FA conjugation, facilitating OXA loading. As reported in studies, the application of the functionalized Fe_3O_4 NPs using CTAB surfactant [53,54] paved the pathway for the preparation of coated NPs for the application in TDD and CDR by MRP. However, using CTAB at high quantities (≥0.01 M) and at high temperature (~80 °C) showed reduction in crystallinity and saturation magnetization. The removal of CTAB by calcination [54] was found to cause high aggrega-

tion and increase the instability index value. Herein, our work attempts to further improve the reported protocol following optimized steps, including keeping the surfactant until the addition of NH_2 groups. This led to reduced aggregation, as well as improved thermal and dispersion stability of the NPs. Accordingly, the CTAB surfactant was removed via the reflux of Fe_3O_4@CTAB-SiO_2-NH_2 NPs which completely degraded the CTAB, leading to a mesoporous structure. This aligns consistently with the reported literature [51]. As such, our successful procedure for removing the CTAB could be beneficial for increasing the surface area of the functionalized NPs which can ease the process for OXA loading.

3.1. Physicochemical Characterization of Nanoparticles

3.1.1. FT-IR Spectroscopy

FT-IR was applied to validate the stepwise surface functionalization of Fe_3O_4 NPs with SiO_2, NH_2, and FA. The spectra of Fe_3O_4@CTAB-SiO_2, Fe_3O_4@CTAB-SiO_2-NH_2, Fe_3O_4@MSN-NH_2, and Fe_3O_4@MSN-NH_2/FA are shown in Figure 3a(i–iv), respectively. The spectrum of Fe_3O_4@CTAB-SiO_2 (Figure 3a(i)) displays a broad band at ~3400 cm^{-1}, attributing to O-H stretching from adsorbed water or surface hydroxyl groups. Peaks at 2925 cm^{-1} and 2854 cm^{-1} are associated with the C-H stretching vibration from the alkyl chain of CTAB. A band at 1637 cm^{-1} corresponded to the scissoring/bending vibration of adsorbed water (H-O-H bending). The strong peak at 1039 cm^{-1} is associated with asymmetric stretching of Si-O-Si bonds, while the peak at 1473 cm^{-1} arises from C-H bending vibrations. The Fe-O vibrations are visible at 630 cm^{-1}. Following the addition of APTES (Figure 3a(ii) Fe_3O_4@CTAB-SiO_2-NH_2), the particles maintained their C-H stretching bands at 2925 cm^{-1} and 2854 cm^{-1}. The appearance of new signals at 1554 cm^{-1} and 1546 cm^{-1} is assigned to N-H bending and confirms the successful addition of amine groups. The Si-O-Si stretch remains visible at 1039 cm^{-1}. In the spectrum of Fe_3O_4@MSN-NH_2 (Figure 3a(iii), the absence of C-H stretching bands at 2925 cm^{-1} and 2854 cm^{-1} confirms successful surfactant (CTAB) removal. Upon FA conjugation (Figure 3a(iv), Fe_3O_4@MSN-NH_2/FA), new peaks appear at 3558 cm^{-1}, 3487 cm^{-1}, 3407 cm^{-1}, and 3224 cm^{-1}. Peaks at 3558 cm^{-1} and 3487 cm^{-1} are a result of free primary amine (NH_2) stretching vibrations of the pteridine ring of FA. The peak at 3407 cm^{-1} contributes to N-H stretching of the pteridine ring in FA involved in hydrogen bonding. The peak at 3224 cm^{-1} suggests the presence of secondary amide N-H stretching, confirming the successful formation of covalent amide bond between the surface MSN-NH_2 and the FA. A prominent peak at 1616 cm^{-1} corresponds to primary amide C=O stretching vibration which overlapped with the characteristic primary amine bending of the pteridine ring in FA. The Si-O-Si peak at 1060 cm^{-1} becomes weaker due to surface shielding and chemical modifications introduced by FA. The Fe-O band at 630 cm^{-1} becomes sharper following FA conjugation, likely due to improved structural organization and decreased interference from surface-adsorbed species. Table 1 summarizes the frequency assignments and wavenumbers reported in this study.

Table 1. FT-IR spectral analysis of Fe_3O_4@CTAB-SiO_2, Fe_3O_4@CTAB-SiO_2-NH_2, Fe_3O_4@MSN-NH_2, and Fe3O4@MSN-NH2/FA.

Samples	Functional Group	Wavenumber (cm^{-1})	Assignment	Ref.
Fe_3O_4@MSN-NH_2/FA	N-H	3558	Primary amine stretching of FA pteridine ring	[63–65]
	N-H	3487		
	N-H	3407	N-H stretching of FA pteridine ring (H-bonding)	
	N-H	3224	Secondary amide N-H stretching	

Table 1. *Cont.*

Samples	Functional Group	Wavenumber (cm^{-1})	Assignment	Ref.
Fe_3O_4@CTAB-SiO_2, Fe_3O_4@CTAB-SiO_2-NH_2	C-H	2925, 2854	Asymmetric and symmetric C-H stretching of CTAB alkyl chains	[65,66]
Fe_3O_4@CTAB-SiO_2	H-O-H	1637	Scissoring/bending vibration of adsorbed water	[67]
Fe_3O_4@MSN-NH_2/FA	C=O	1616	Primary amide band (C=O stretching) overlapping with FA primary amine bending	[65]
Fe_3O_4@CTAB-SiO_2-NH_2, Fe_3O_4@MSN-NH_2	N-H	1554–1527	N-H bending of surface primary amines	[61,63,65,67,68]
Fe_3O_4@CTAB-SiO_2	C-H	1473	Alkyl group bending from CTAB	[63,66]
All samples	Si-O-Si	1083–1039	Asymmetric stretching	[63,69]
All samples	Si-O	800	Symmetric stretching	[61,69]
All samples	Fe-O	630	Stretching vibration of the octahedral Fe-O in Fe_3O_4	[60]

The progressive evolution of FT-IR spectra validates the successful synthesis of multi-functionalized Fe_3O_4 NPs. The persistence of Fe-O vibration at 630 cm^{-1} and the Si-O-Si bands across all synthesis steps (Fe_3O_4@CTAB-SiO_2, Fe_3O_4@CTAB-SiO_2-NH_2, Fe_3O_4@MSN-NH_2, and Fe_3O_4@MSN-NH_2/FA) suggest that the core–shell inorganic structure remains intact despite multiple chemical modifications. The transition from a surfactant (CTAB)-filled SiO_2 shell to a mesoporous structure is evidenced by the disappearance of alkyl C-H stretching bands at 2925 and 2854 cm^{-1}. This is the most critical stage not only for facilitating drug loading but also for reducing cell cytotoxicity associated with residual CTAB. The appearance of N-H bending signals (1554 and 1546 cm^{-1}) confirms successful surface functionalization with primary amines by silanization, facilitating the necessary anchors for ligand attachment. Subsequent FA conjugation is confirmed by the appearance of the secondary amide N-H stretch at 3224 cm^{-1} and the primary amide band at 1616 cm^{-1}, indicating covalent FA attachment. Such robust covalent linkages guarantee stability during systemic circulation. Furthermore, the presence of the pteridine ring fingerprints (3558 cm^{-1}, 3487 cm^{-1}, 3407 cm^{-1}) indicates that FA retains its structural integrity during coupling process. The observed FT-IR wavenumbers align well with those reported in the literature [60,63,65–68], validating the successful modification of Fe_3O_4 NPs.

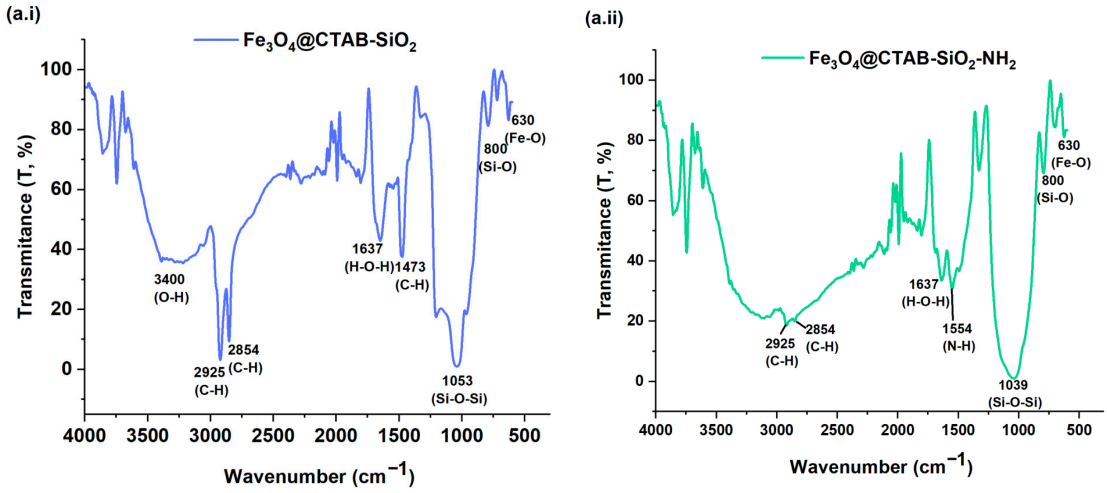

Figure 3. *Cont.*

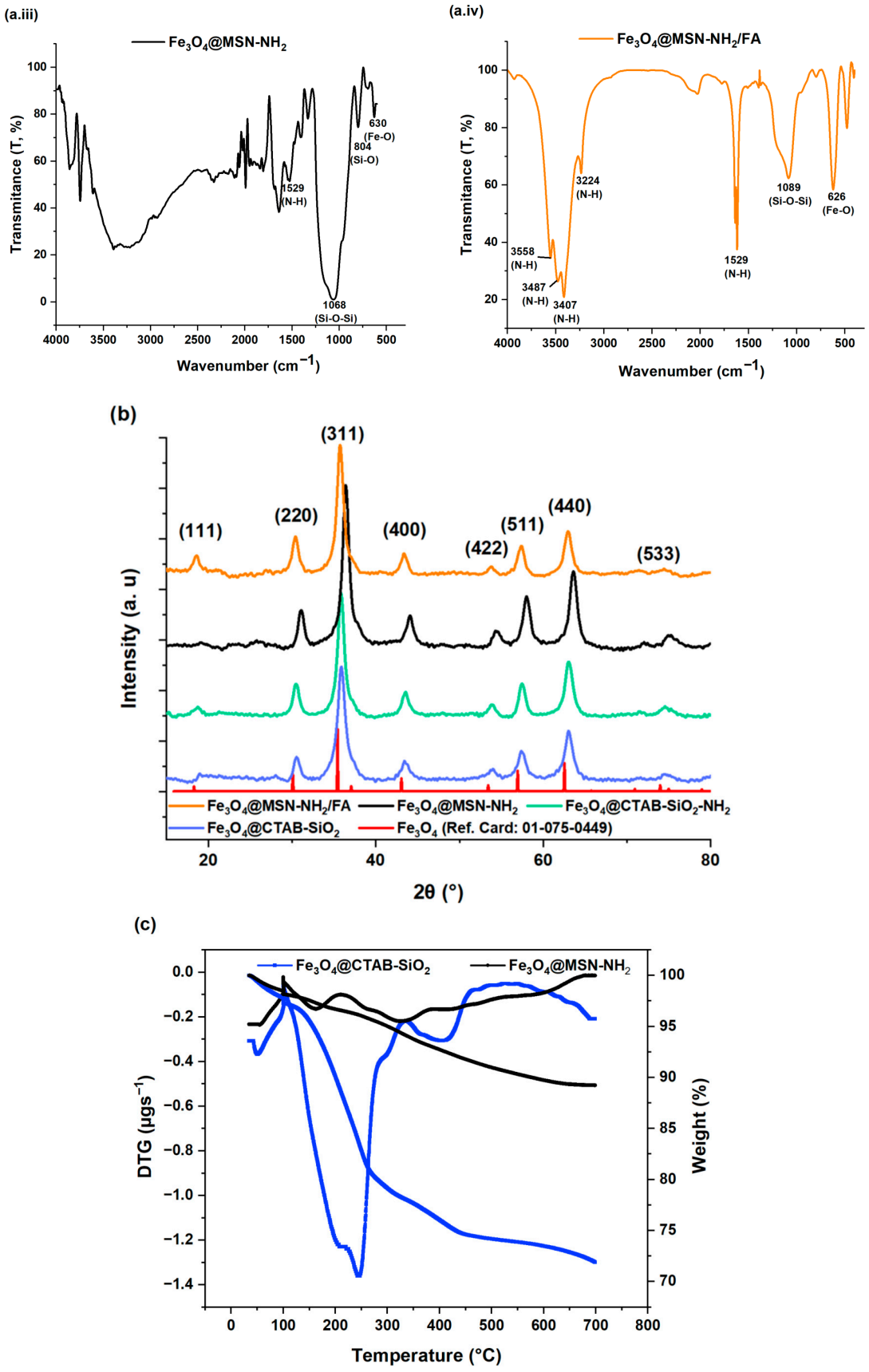

Figure 3. (**a**(**i**)–**a**(**iv**)) FT-IR of Fe_3O_4@CTAB-SiO_2, Fe_3O_4@CTAB-SiO_2-NH_2, Fe_3O_4@MSN-NH_2, and Fe_3O_4@MSN-NH_2/FA. (**b**) PXRD of synthesized Fe_3O_4@CTAB-SiO_2, Fe_3O_4@CTAB-SiO_2-NH_2, Fe_3O_4@MSN-NH_2, Fe_3O_4@MSN-NH_2/FA NPs, and ICDD PDF card no. 01-075-0449. (**c**) TGA/DTG spectra of Fe_3O_4@CTAB-SiO_2 and Fe_3O_4@MSN-NH_2.

3.1.2. Powder X-Ray Diffraction (PXRD)

PXRD spectra of Fe_3O_4@CTAB-SiO_2, Fe_3O_4@CTAB-SiO_2-NH_2, Fe_3O_4@MSN-NH_2, and Fe_3O_4@MSN-NH_2/FA are shown in Figure 3b, respectively. All samples displayed diffraction peaks at the (111), (220), (311), (400), (422), (511), (440), and (533) crystal planes. The peaks correspond to the diffraction pattern of Fe_3O_4, which is in excellent agreement with ICDD PDF card no. 01-075-0449 and the literature [60].

PXRD patterns of Fe_3O_4@CTAB-SiO_2, Fe_3O_4@CTAB-SiO_2-NH_2, Fe_3O_4@MSN-NH_2, and Fe_3O_4@MSN-NH_2/FA displayed similar diffraction peaks, corresponding to F_3O_4. This indicates that the spinel crystal structure of the core was preserved throughout coating, functionalization, and FA conjugation with no evidence of lattice alteration or secondary phase formation. Similarly, Ni et al. [65] observed that Fe_3O_4@MSN-NH_2/FA maintained their diffraction peaks during FA conjugation and even after paclitaxel loading, confirming structural robustness as this is critical for retaining magnetic characteristics and drug delivery performance [65].

3.1.3. Thermogravimetric and Derivative Thermogravimetric Analysis

The TGA and DTG curves for Fe_3O_4@CTAB-SiO_2 and Fe_3O_4@MSN-NH_2 are displayed in Figure 3c. Both samples showed pronounced weight loss patterns at various temperature regions. As seen, the initial weight loss at a temperature range of ~30–120 °C was attributed to thermal release of the residual water or moisture and other solvents, consistent with the literature [70]. The TGA curves of Fe_3O_4@CTAB-SiO_2 contain four weight loss phases where the second phase of weight loss between ~110 and 300 °C accounted for 19.02% of the total weight loss. This major loss is ascribed to the decomposition of CTAB, similar to the literature [71]. In contrast, a major loss cannot be seen in the case of Fe_3O_4@MSN-NH_2 which supports the removal of CTAB from NPs. Between ~350–700 °C, a smaller weight loss of ~7% was observed, which corresponds to the thermal degradation of APTES molecules. DTG curves supported these findings, exhibiting multiple decomposition stages within the range of 100–400 °C for Fe_3O_4@CTAB-SiO_2 and Fe_3O_4@MSN-NH_2. The detailed thermal data for both samples are summarized in Supplementary Information Table S3.

The thermal studies of Fe_3O_4@CTAB-SiO_2 and Fe_3O_4@MSN-NH_2 by TGA/DTG verifies the synthetic pathway removed CTAB from NPs' surface. The absence of major weight loss in the 110–300 °C range for Fe_3O_4@MSN-NH_2 supports CTAB decomposition/removal. Jin et al. [72] demonstrated that the residual surfactant can induce cytotoxicity in vitro and in vivo [72]. A minor weight loss was seen between 350 and 700 °C, attributed to the degradation of APTES molecules, confirming successful amine functionalization. These observations align with previously reported studies on mesoporous silica-coated Fe_3O_4 NPs, where removal of CTAB and surface functionalization are vital to obtain colloidal stability and biocompatibility [70,71].

3.1.4. X-Ray Photoelectron Spectroscopy

XPS was used to study the chemical state and electronic environment of Pt species in OXA-loaded samples, Fe_3O_4@MSN-NH_2/OXA and Fe_3O_4@MSN-NH_2/FA/OXA, as shown in Figures 4a and 4b, respectively. The Pt 4f spectra for each sample were collected in 10 sweeps with a step size of 0.1 eV, a dwell time of 0.2 s, and a pass energy of 30 eV. Peak fitting was performed using the CasaXPS software (Version 2.3.24, Casa Software Ltd., Teignmouth, UK). with a Gaussian–Lorentzian peak shape (70:30) and a Shirley background. The Pt 4f peaks have two peaks for each chemical state resulting from spin–orbit coupling. This splitting has a distinctive intensity ratio (4:3) and energy separation of approximately 3.3 eV. In the Fe_3O_4@MSN-NH_2/OXA sample, deconvolution of the Pt 4f region (Figure 4a) shows two distinct oxidation states. The Pt $4f_{7/2}$ at 73.59 eV corresponds to partially

reduced Pt species (Pt^{2+} or Pt^{0}), and Pt $4f_{7/2}$ peak at 77.57 eV can be assigned to oxidized Pt^{4+} species. Signal-to-noise ratio was relatively high due to low Pt loading, which limited the significance of this interpretation. Whereas in Fe_3O_4@MSN-NH_2/FA/OXA sample (Figure 4b), a single chemical environment was observed, with the corresponding Pt $4f_{7/2}$ and Pt $4f_{5/2}$ peaks arising from the same oxidation state.

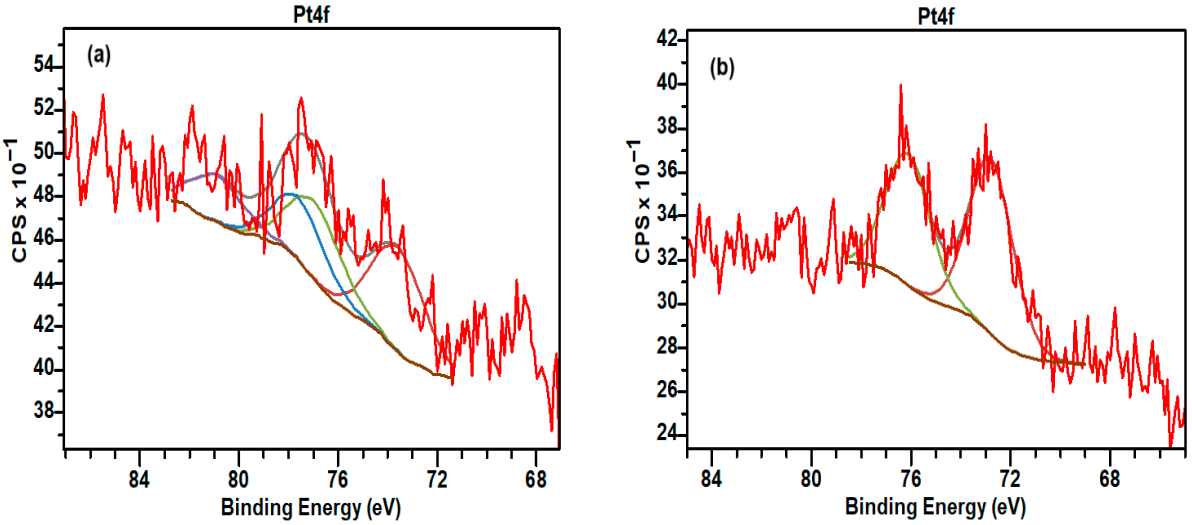

Figure 4. XPS spectra of Pt environment of (**a**) Fe_3O_4@MSN-NH_2/OXA and (**b**) Fe_3O_4@MSN-NH_2/FA/OXA.

The XPS results showed significant variations in the chemical environment of platinum between Fe_3O_4@MSN-NH_2/OXA and Fe_3O_4@MSN-NH_2/FA/OXA formulations. In Fe_3O_4@MSN-NH_2/OXA (Figure 4a), the presence of two Pt oxidation states reveals heterogenous Pt coordination on the amine-functionalized surface. The partially reduced Pt species (Pt^{2+} or Pt^{0}) are likely linked to interaction between electron-donating groups on the surface (e.g., amines) and OXA which may have facilitated partial reduction or ligand exchange [73]. The higher binding energy component (Pt $4f_{7/2}$ peak at 77.57 eV) is attributed to oxidized Pt^{4+} species, which is consistent with previously reported XPS signatures of OXA-derived Pt environments [74]. In contrast, a single chemical environment in the Fe_3O_4@MSN-NH_2/FA/OXA sample reveals a more homogeneous Pt coordination state, with the Pt $4f_{7/2}$ and Pt $4f_{5/2}$ peaks originating from the same oxidation state. The Pt $4f_{7/2}$ at 72.8 eV is characteristic of the platinum hydroxide species, parallel to the literature [75]. This highlights that under the mild experimental conditions, OXA may have partially dechelated, exposing a reactive Pt site to coordinate with electron-donating groups, such as amine groups or hydroxyl groups present in folic acid.

3.1.5. Transmission Electron Microscopy

Figure 5 shows TEM images of the Fe_3O_4@MSN-NH_2/FA/OXA sample. The TEM images (Figure 5a(i–iii)) exhibited quasi-spherical morphology. The magnetic core size was approximately 7 nm and the overall particle diameter expanded to 14 ± 2 nm after the functionalization and OXA loading (Figure 5d). Selected area electron diffraction (SAED) (Figure 5a(iv)) patterns showed a series of distinct diffraction rings corresponding to magnetite lattice planes, validating the polycrystalline nature and crystalline structure of the Fe_3O_4 core. Energy dispersive X-ray spectroscopy (EDX) mapping confirmed silica coating around the Fe_3O_4 core, forming a core–shell structure (Figure 5b(i)). The EDX spectrum further verified the elemental composition of Fe_3O_4@MSN-NH_2/FA/OXA (Figure 5c).

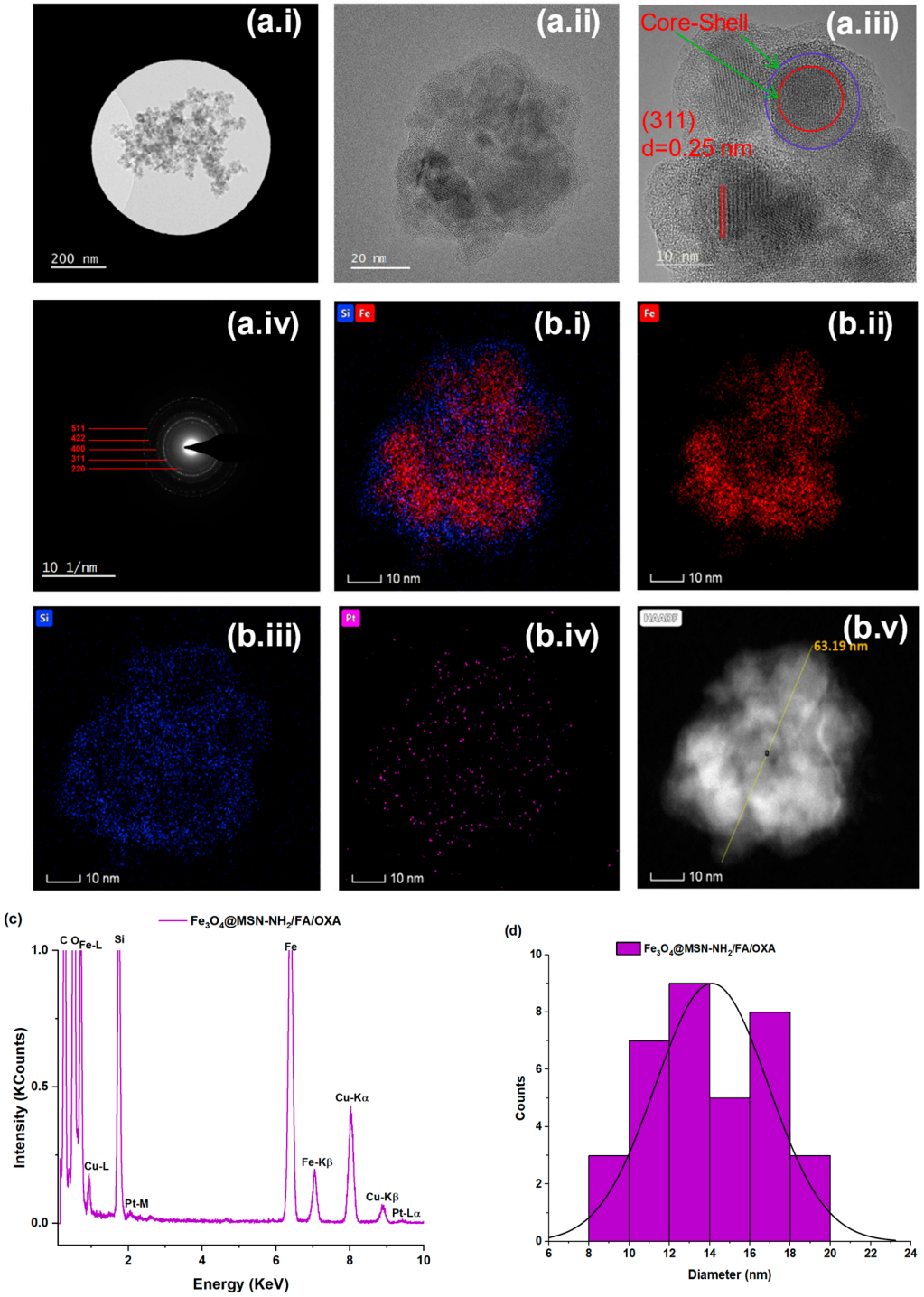

Figure 5. (**a**) High-resolution TEM images (HR-TEM) of Fe_3O_4@MSN-NH_2/FA/OXA; (**a**(**i**)) HR-TEM; (**a**(**ii**,**iii**)) zoomed view; (**a**(**iv**)) SAED pattern; (**b**) EDX mapping: (**b**(**i**)) core–shell, (Si and Fe), (**b**(**ii**)) Fe, (**b**(**iii**)) Si, (**b**(**iv**)) Pt, (**b**(**v**)) HADDF; (**c**) EDX spectrum; (**d**) particle size distribution.

The TEM analysis confirms the formation of a core–shell structure, where SiO_2 coating provides structural stability and reduces Fe_3O_4 aggregation. The increase in diameter from 7 nm (core) to 14 ± 2 nm after FA conjugation and OXA loading indicates effective surface modification and drug incorporation. SAED patterns verify the crystalline integrity of the NPs post-functionalization, which is essential for retaining magnetic responsiveness. EDX mapping exhibits a consistent silica shell and EDX spectrum confirms the incorporation of FA and OXA onto Fe_3O_4@MSN-NH_2 surface.

3.1.6. Brunauer–Emmett–Teller Surface Area and Porosity Analysis

The specific surface areas of Fe_3O_4@MSN-NH_2, Fe_3O_4@MSN-NH_2/OXA, Fe_3O_4@MSN-NH_2/FA, and Fe_3O_4@MSN-NH_2/FA/OXA were analyzed by BET nitrogen adsorption–desorption isotherms at 77 K, measured against relative pressure (P/P0) at 77 K. Prior to analysis, the samples were degassed by heating to 60 °C at a rate of 5.0 °C/min for 1 h, followed by further heating to 100 °C at the same rate for 15 h. All samples demonstrated somewhat hysteresis loops, suggestive of mesoporous structure with minor micropores and cylindrical-shaped pores (Figure 6). As expected, the removal of CTAB generated mesoporosity in Fe_3O_4@MSN-NH_2 NPs, which exhibited the highest surface area of 419.95 m^2/g and the micropore volume of 0.086 cm^3/g. Functionalization with FA (Fe_3O_4@MSN-NH_2/FA) significantly reduced the surface area to 40.33 m^2/g, likely due to surface coverage and decreased pore accessibility. The surface area of OXA-loaded samples, Fe_3O_4@MSN-NH_2/OXA and Fe_3O_4@MSN-NH_2/FA/OXA, was slightly higher than that of FA functionalized (Fe_3O_4@MSN-NH_2/FA) at 189.06 m^2/g and 184.66 m^2/g, respectively.

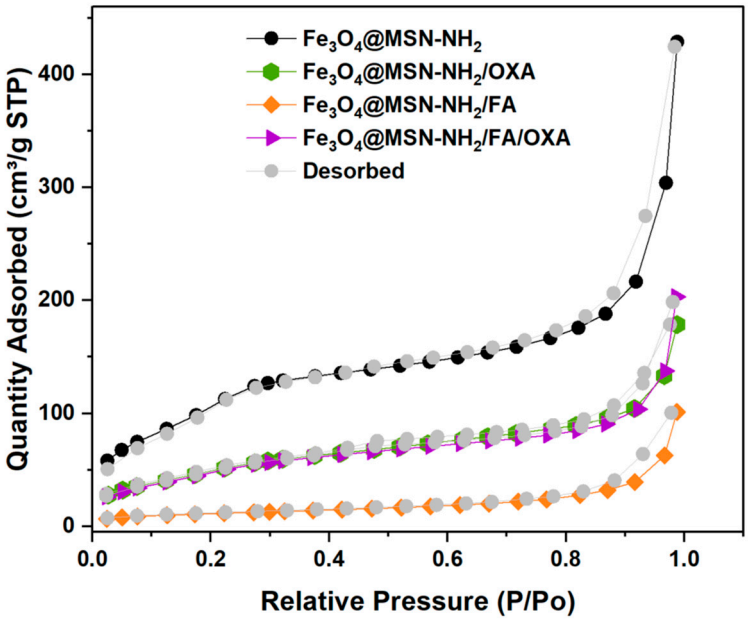

Figure 6. N_2 adsorption–desorption isotherms for the BET surface area analyses of Fe_3O_4@MSN-NH_2, Fe_3O_4@MSN-NH_2/OXA, Fe_3O_4@MSN-NH_2/FA, and Fe_3O_4@MSN-NH_2/FA/OXA.

The BET analysis demonstrates that the removal of the CTAB surfactant is vital to generating mesoporosity, as highlighted by the high surface area of Fe_3O_4@MSN-NH_2 (419.95 m^2/g). The significant reduction in surface area following FA conjugation (40.33 m^2/g) suggests that bulky FA molecules block pore openings and mask available surface sites, which is consistent with a ligand-functionalized mesoporous silica network [76]. Notably, OXA loading partially recovers surface area in both Fe_3O_4@MSN-NH_2/OXA and Fe_3O_4@MSN-NH_2/FA/OXA formulations (189.06 m^2/g and 184.66 m^2/g), which may suggest that OXA molecules adhere to the external surfaces of the NPs instead of penetrating internal mesopores. The findings are fundamental for understanding OXA loading efficiency and release profile.

3.1.7. Dispersion Stability and Colloidal Properties

The dispersion stability of Fe_3O_4@MSN-NH_2, Fe_3O_4@MSN-NH_2/FA, Fe_3O_4@MSN-NH_2/OXA, and Fe_3O_4@MSN-NH_2/FA/OXA in PBS was measured by the LUMiSizer technique at different temperatures: 4 °C (storage), 25 °C (ambient), 37 °C (physiological), and 43 °C (hyperthermia conditions). The instability index, a dimensionless value between

zero (highly stable) and one (highly unstable), highlights the tendency of NPs to aggregate/sediment under centrifugal force, providing insight into colloidal behavior under varied conditions [61]. The results are summarized in Table 2 and dispersion profiles at 25 °C are shown in Figure 7a. Among the formulations, Fe_3O_4@MSN-NH_2/FA displayed an instability index, exceeding one at 25 °C, while Fe_3O_4@MSN-NH_2/FA/OXA exhibited improved stability across all tested temperatures, and, in particular, at 43 °C, where it outperformed Fe_3O_4@MSN-NH_2/OXA.

Table 2. Dispersion stability of Fe_3O_4@MSN-NH2, Fe_3O_4@MSN-NH_2/OXA, Fe_3O_4@MSN-NH_2/FA and Fe_3O_4@MSN-NH_2/FA/OXA in PBS at 4 °C, 25 °C, 37 °C, and 43 °C by LUMiSizer technique.

Sample Name	Instability Index (4 °C)	Instability Index (25 °C)	Instability Index (36 °C)	Instability Index (43 °C)
Fe_3O_4@MSN-NH_2	0.94 ± 0.07	0.79 ± 0.06	0.88 ± 0.05	0.57 ± 0.05
Fe_3O_4@MSN-NH_2/OXA	0.82 ± 0.05	0.90 ± 0.03	0.99 ± 0.06	0.91 ± 0.03
Fe_3O_4@MSN-NH_2/FA	0.83 ± 0.07	1.03 ± 0.09	0.87 ± 0.06	0.76 ± 0.07
Fe_3O_4@MSN-NH_2/FA/OXA	0.80 ± 0.06	0.81 ± 0.05	0.88 ± 0.07	0.51 ± 0.07

Based on LUMiSizer results, FA conjugation independently impacts colloidal stability, likely due to its solubility behavior and shielding of surface charges, which weakens the electrostatic repulsion between NPs [61]. In contrast, the addition of OXA considerably enhances stability, especially under hyperthermic conditions (43 °C). This stabilization is likely due to the contribution of OXA in intermolecular interactions, leading to a reduction in NP aggregation. Overall, the conjugation of FA and OXA onto Fe_3O_4@MSN-NH_2 led to better dispersion stability, in particular, above room temperature, supporting their suitability for physiological environments and potential application in hyperthermia-based therapy.

3.1.8. Dynamic Light Scattering and Zeta Potential

DLS, zeta potential, and polydispersity index (PDI) measurements were applied to determine the colloidal characteristics of the NPs, including their hydrodynamic size, and surface charge in dispersion systems (Figure 7b,c). The hydrodynamic sizes and PDI (shown in brackets) of the Fe_3O_4@MSN-NH_2, Fe_3O_4@MSN-NH_2/OXA, Fe_3O_4@MSN-NH_2/FA, and Fe_3O_4@MSN-NH_2/FA/OXA were 69 ± 7 nm (0.116), 60 ± 5 nm (0.101), 80 ± 9 nm (0.119) and 93 ± 15 nm (0.113), respectively.

The zeta potential of Fe_3O_4@MSN-NH_2, Fe_3O_4@MSN-NH_2/OXA, Fe_3O_4@MSN-NH_2/FA, and Fe_3O_4@MSN-NH_2/FA/OXA were 17.35 mV, −32.62 mV, −18.75 mV, and −51.22 mV, respectively. The hydrodynamic size, surface zeta potential, and PDI data of Fe_3O_4@MSN-NH_2, Fe_3O_4@MSN-NH_2/OXA, Fe_3O_4@MSN-NH_2/FA, and Fe_3O_4@MSN-NH_2/FA/OXA are summarized in Table 3.

DLS analysis revealed an increase in hydrodynamic size following FA conjugation and OXA loading. The increase in size may be as a result of the formation of the hydration shell due to the interaction between surface functional groups on Fe_3O_4 NPs with surrounding water molecules, during DLS measurements. The low PDI values (<0.12) observed across all formulations indicate good monodispersity and colloidal stability, which are essential for consistent OXA delivery. The slight increase in hydrodynamic size and PDI for the FA and OXA-functionalized NPs points to successful conjugation and steric hindrance introduced by these moieties.

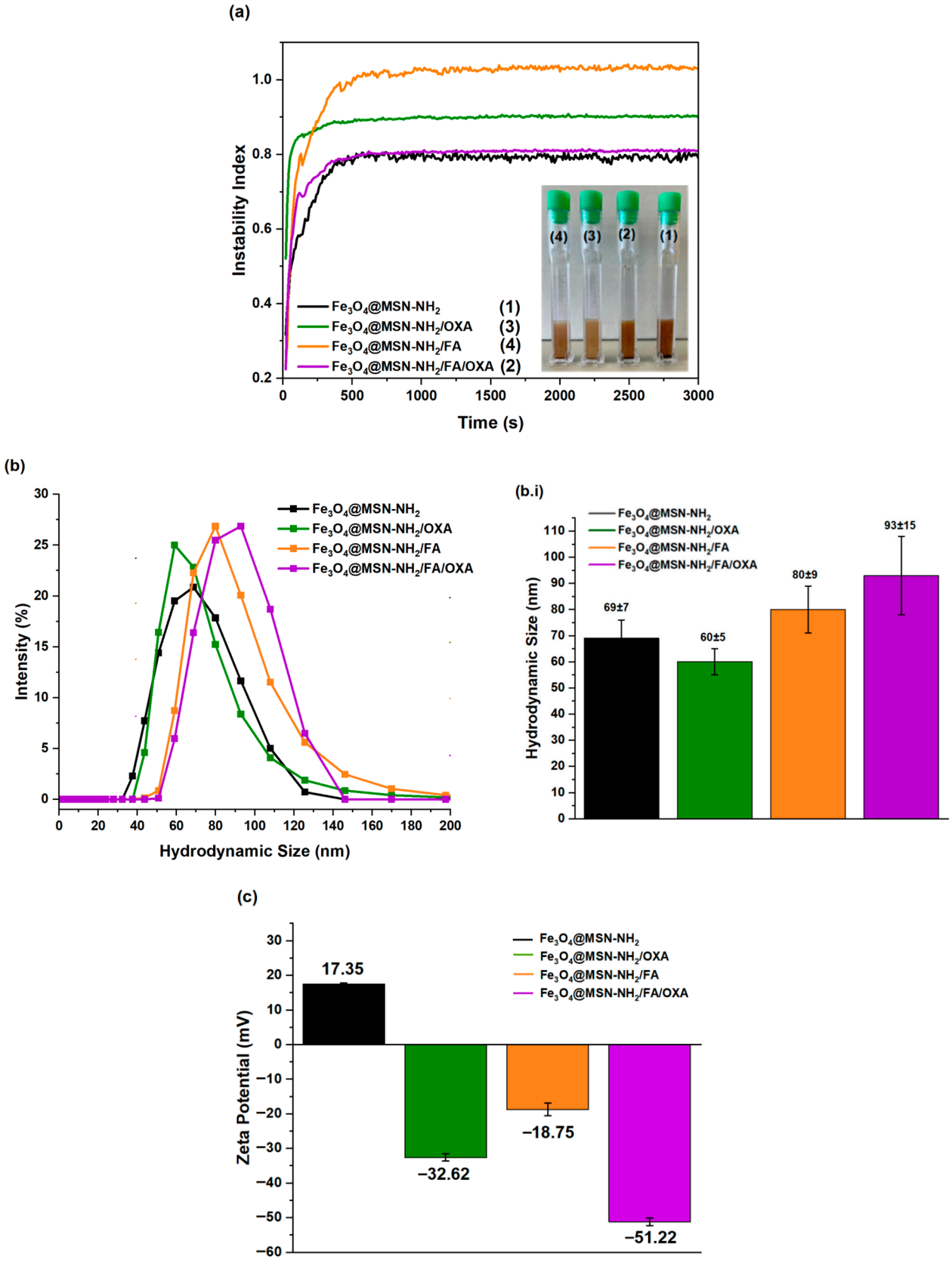

Figure 7. (**a**) Dispersion stability of Fe_3O_4@MSN-NH_2, F_3O_4@MSN-NH_2/OXA, Fe_3O_4@MSN-NH_2/FA, and Fe_3O_4@MSN-NH_2/FA/OXA at 25 °C. (**b**,**b**(**i**)) Hydrodynamic size and (**c**) surface zeta potential of Fe_3O_4@MSN-NH_2, F_3O_4@MSN-NH_2/OXA, Fe_3O_4@MSN-NH_2/FA, and Fe_3O_4@MSN-NH_2/FA/OXA.at 25 °C.

Table 3. Hydrodynamic size, zeta potential, and PDI of Fe_3O_4@MSN-NH_2, F_3O_4@MSN-NH_2/OXA, Fe_3O4@MSN-NH_2/FA, and Fe_3O_4@MSN-NH_2/FA/OXA at 25 °C.

Parameters	Fe_3O_4@MSN-NH_2	Fe_3O_4@MSN-NH_2/OXA	Fe_3O_4@MSN-NH_2/FA	Fe_3O_4@MSN-NH_2/FA/OXA
Hydrodynamic size (nm)	69 ± 7	60 ± 5	80 ± 9	93 ± 15
Zeta potential (mV)	+17.45 ± 2	−32.6 ± 1.3	−18.76 ± 1.8	−51.2 ± 1.5
PDI	0.116	0.101	0.119	0.113

Zeta potential measurements provide understanding on how surface functionalization impacts electrostatic behavior and colloidal stability. In general, particles with a magnitude of greater than ±30 mV are considered to have good colloidal stability as the repulsive electrostatic forces between particles help to suppress the attractive forces, preventing aggregation and rapid sedimentation [77]. Fe_3O_4@MSN-NH_2 (+17.35 mV) displays moderate stability, while OXA loading noticeably shifts to a negative surface charge (−32.62 mV), improving electrostatic repulsion and minimizing aggregation. FA conjugation alone minimized surface charge (Fe_3O_4@MSN-NH_2/FA −18.76 mV), likely due to FA's zwitterionic profile (containing acidic (-OH) and the basic (-NH_2) functional groups) and the bulky structure of FA masking ionizable surface groups (e.g., NH_2, Si-OH). This effect correlates with the instability index obtained by LUMiSizer analysis (Section 3.1.7), where the Fe_3O_4@MSN-NH_2/FA sample demonstrated a higher instability index at 25 °C. The Fe_3O_4@MSN-NH_2/FA/OXA sample demonstrated the highest magnetite of zeta potential value at −51.22 mV. This substantial increase from −18.76 mV (observed in Fe_3O_4@MSN-NH_2/FA) was primarily due to the chemical structure of OXA. Upon OXA loading, the negative oxalate ligands in OXA likely contributed extra surface charges, increasing the overall negative potential. This led to stronger electrostatic repulsion between NPs, thereby enhancing colloidal stability and decreasing the likelihood of aggregation. As revealed by XPS analysis (Section 3.1.4), OXA may have partially dechelated, exposing its Pt center to coordinate with electron-donating groups (-NH_2) and hydroxyl groups from FA. This coordination likely modified the surface charge, leading to an increased negative zeta potential. Also, FA and OXA collectively may have introduced steric hindrance and enhanced electrostatic repulsion, which amplified surface charge. The significantly high negative zeta potential (−51.22 mV) suggests stronger electrostatic repulsion between particles, which aligns with the improved colloidal stability observed in dispersion studies by LUMiSizer (Section 3.1.7).

3.2. Magnetic Properties

3.2.1. Magnetization and Superparamagnetic Properties

The magnetic properties of the prepared samples were measured using SQUID-VSM at 300 K. As presented in Table 4, all samples showed negligible coercivity (Hc ~0.00012–0.00142 T) and low remanent magnetization (Mr/Ms ≤ 0.02). The saturation magnetization (Ms) values of Fe_3O_4, Fe_3O_4@CTAB-SiO_2, Fe_3O_4@CTAB-SiO_2-NH_2, Fe_3O_4@MSN-NH_2, Fe_3O_4@MSN-NH_2/OXA, Fe_3O_4@MSN-NH_2/FA, and Fe_3O_4@MSN-NH_2/FA/OXA NPs were 78.50 emu/g, 27.50 emu/g, 58.84 emu/g, 61.12 emu/g, 55.35 emu/g, 37.48 emu/g, and 38.55 emu/g, respectively. The complete magnetic parameters for all samples are collected in Table 4; Figure 8a,b illustrates saturation magnetization curves for Fe_3O_4@MSN-NH_2, Fe_3O_4@MSN-NH_2/OXA, Fe_3O_4@MSN-NH_2/FA, and Fe_3O_4@MSN-NH_2/FA/OXA samples at 300 K.

Table 4. Magnetic properties of the synthesized NPs at 300 K.

Samples	Fe_3O_4	Fe_3O_4@CTAB-SiO_2	Fe_3O_4@CTAB-SiO_2-NH_2	Fe_3O_4@MSN-NH_2	Fe_3O_4@MSN-NH_2/OXA	Fe_3O_4@MSN-NH_2/FA	Fe_3O_4@MSN-NH_2/FA/OXA
Hc (T)	0.00060 (2)	0.00142 (2)	0.00040 (2)	0.00048 (2)	0.00038 (2)	0.00012 (2)	0.00023 (2)
Mr (emu/g)	0.664	0.548	0.385	0.398	0.316	0.229	0.1098
Ms (emu/g)	78.50	27.52	58.85	61.24	55.35	37.48	38.55
Mr/Ms	0.00846	0.01991	0.00654	0.00650	0.00571	0.00610	0.00495

Remnant magnetization (Mr); coercive field (Hc); saturation magnetization (Ms); remnant magnetization (emu/g)/saturation magnetization (emu/g) (Mr/Ms). For Hc values, uncertainty is shown based on instrument precision, while other parameters (Mr, Ms, Mr/Ms) exhibited negligible uncertainty compared to their magnitude and are displayed as mean values.

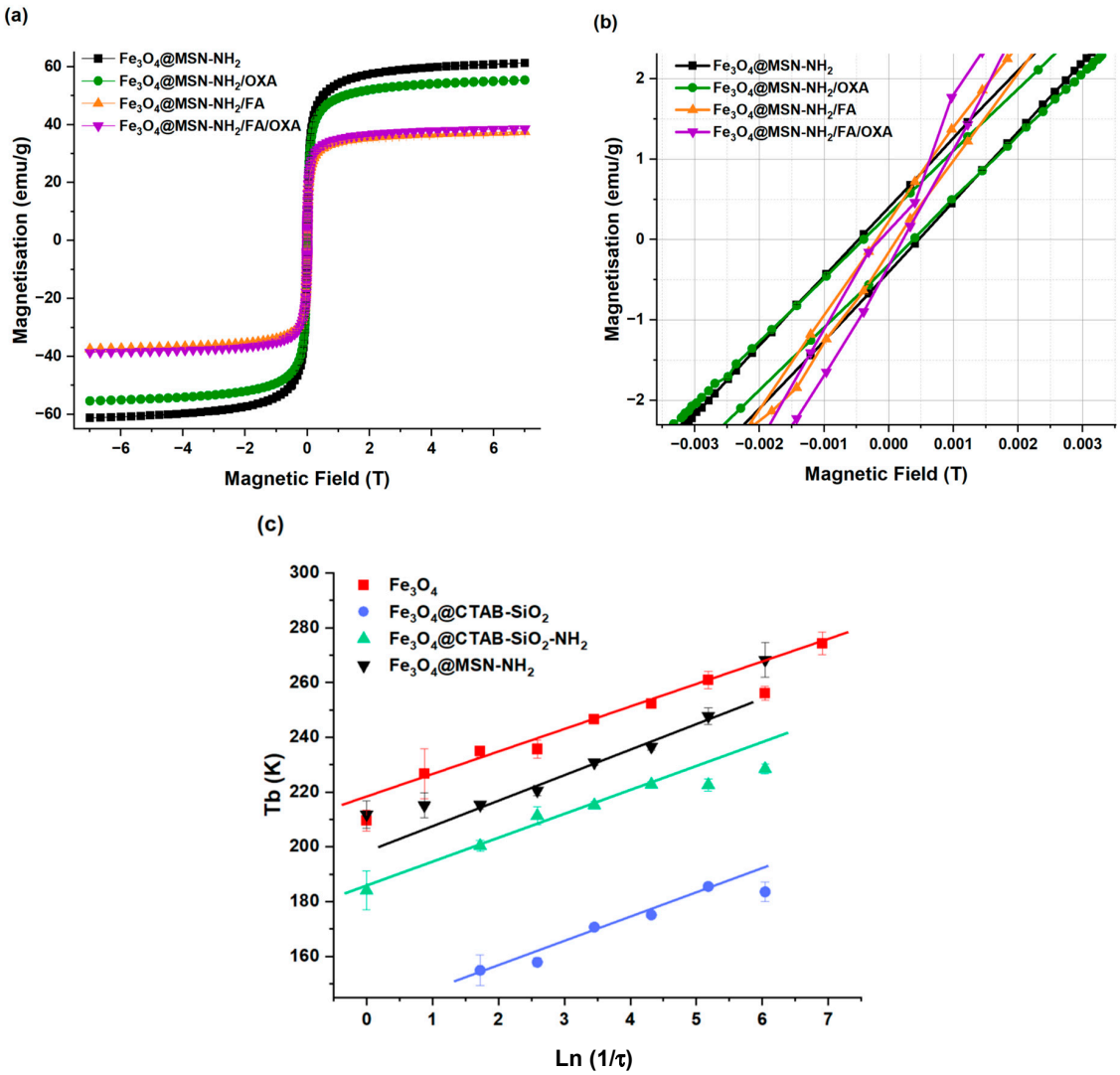

Figure 8. (**a**,**b**) Magnetization hysteresis loop of Fe_3O_4@MSN-NH_2, F_3O_4@MSN-NH_2/OXA, Fe3O4@MSN-NH_2/FA, and Fe_3O_4@MSN-NH_2/FA/OXA. (**c**) Frequency dependence of the blocking temperature of Fe_3O_4, Fe_3O_4@CTAB-SiO_2, Fe_3O_4@CTAB-SiO_2-NH_2, and Fe_3O_4@MSN-NH_2.

3.2.2. Frequency Dependence of the Blocking Temperature

The blocking temperature (Tb) was obtained from the peak position of the imaginary component of AC susceptibility (ACX″) versus temperature. ACX″ data for Fe_3O_4, Fe_3O_4@CTAB-SiO_2, Fe_3O_4@CTAB-SiO_2-NH_2, and Fe_3O_4@MSN-NH_2 are provided in the Supplementary Information Section (Figure S1), where each sample exhibits a characteristic Tb corresponding to ACX″.

To analyze the magnetic relaxation dynamics and the frequency dependence of the Tb, the natural logarithm of the inverse relaxation time ($\ln(1/\tau)$) was plotted against Tb (K), as shown in Figure 8c (the mathematical calculations are collected in Supplementary Information Table S4).

The Nèel–Brown equation was used to extract relaxation parameters [78]:

$$\tau = \tau_0 exp(\frac{U}{k_B T}) \quad (1)$$

where

τ = relaxation time

τ_0 = attempt time

U = magnetic anisotropy energy barrier

K_B = Boltzmann constant (1.380×10^{-23} J/K)

T = temperature (K)

Negligible coercivity (field strength needed to reverse magnetization to zero after saturation) and low remanent magnetization (magnetization remaining after removal of external magnetic field) indicate minimal interparticle magnetic exchange and weak dipole–dipole interactions, consistent with the previously reported literature [79]. These characteristics confirm superparamagnetic nature, in agreement with the literature [54]. The absence of magnetic remanence indicates that the NPs do not retain magnetization once the external magnetic field is removed, which is essential for biomedical utilization that relies on magnetic responsiveness without permanent magnetization. The significant reduction in saturation magnetization for Fe_3O_4@CTAB-SiO_2 can be attributed to the presence of CTAB, which acts as a non-magnetic dead layer on the NP surface, disrupting spin alignment and weakening magnetic coupling. This phenomenon is consistent with previous studies [50,80,81]. SiO_2 and NH_2 coatings also introduce isolating effects, which can lead to a reduced coercivity as noted in the literature [70,82]. FA conjugation and OXA loading further decreased saturation magnetization due to surface coverage. Nevertheless, the final saturation values (37.48 emu/g and 38.55 emu/g) remain within the effective range for biomedical applications. According to Nguyen et al. [83], Fe_3O_4 NPs with saturation magnetization values as low as 30–40 emu/g have proven effective in biomedical applications, including magnetic targeting, MRI, and magnetic hyperthermia. The S-shaped magnetization curves without appreciable hysteresis (Figure 8a) demonstrate that thermal energy at 300 K is adequate to overcome the magnetic anisotropy energy barrier, resulting in rapid fluctuations of magnetic moment once the external field is removed. This observation confirms the superparamagnetic properties of the synthesized NPs.

The linear trends across the measured temperature range (Figure 8c) confirm that Fe_3O_4, Fe_3O_4@CTAB-SiO_2, Fe_3O_4@CTAB-SiO_2-NH_2, and Fe_3O_4@MSN-NH_2 samples follow a thermally activated relaxation process, enabling calculation of the magnetic anisotropy energy barrier (U) and attempt times (τ_0), applying Arrhenius-based analysis [79]. In single domain NPs, thermal energy facilitates magnetic moment flips across the anisotropy energy barrier (U). Above the Tb, the magnetic relaxation becomes rapid enough that the magnetization averages to zero during measurements, demonstrating superparamagnetic behavior [78,84]. The presence of CTAB decreases magnetic coupling and dipole–dipole interactions by reducing aggregate on and improving colloidal stability. Following the completion of the functionalization and subsequent removal of CTAB, the magnetic behavior, especially saturation magnetization, improved, approaching values observed for uncoated Fe_3O_4 core NPs. The observed frequency-dependent change in Tb indicates the dynamic relaxation results align well with the static magnetization trends (Section 3.2.1), confirming that magnetic characteristics are controlled by thermal activation

rather than strong interparticle exchange coupling. Collectively, these findings confirm that all synthesized NPs demonstrate superparamagnetic profile under the tested conditions.

3.3. MRI Analysis

To evaluate the MRI contrast potential of the synthesized Fe_3O_4-based therapeutic agents, both longitudinal (T1) and transverse (T2) relaxation times were measured at 50 µg/mL and 5 µg/mL concentrations. Across all samples, T2-weighted contrast was the predominant effect, while T1 values remained relatively consistent (~2.25–2.85 s), suggesting minimal influence on longitudinal relaxation. The data are provided in Table 5.

Table 5. Relaxation times (T1 and T2) of the Fe_3O_4@MSN-NH_2, F_3O_4@MSN-NH_2/OXA, Fe_3O4@MSN-NH_2/FA, and Fe_3O_4@MSN-NH_2/FA/OXA at 5 µg/mL and 50 µg/mL concentrations in 1% agarose phantom.

ROI	Samples	[µg/mL]	T1/[s]	T2/[s]
1	Fe_3O_4@MSN-NH_2/FA	50	2.254± 0.047	0.013107 ± 0.00049
2	Fe_3O_4@MSN-NH_2/OXA	50	2.368 ± 0.050	0.03400 ± 0.00084
3	Fe_3O_4@MSN-NH_2	50	2.615 ± 0.064	0.0688 ± 0.0017
4	Fe_3O_4@MSN-NH_2/FA	5	2.818 ± 0.048	0.05624 ± 0.00067
5	Fe_3O_4@MSN-NH_2/FA/OXA	5	2.835 ± 0.055	0.05848 ± 0.00064
6	Fe_3O_4@MSN-NH_2/OXA	5	2.819 ± 0.045	0.08001 ± 0.00079
7	Fe_3O_4@MSN-NH_2	5	2.852 ± 0.054	0.09014 ± 0.00085
8	Fe_3O_4@MSN-NH_2/FA/OXA	50	2.382 ± 0.054	0.01544 ± 0.00050
9	Agarose	-	2.826 ± 0.051	0.07295 ± 0.00063

The T2-map analysis (Figure 9) demonstrated significant contrast enhancement in OXA-loaded and FA-functionalized samples. Notably, at higher concentration (50 µg/mL), Fe_3O_4@MSN-NH_2/FA (ROI 1) showed the shortest T2 at 0.0131 s, followed closely by Fe_3O_4@MSN-NH_2/FA/OXA (ROI 8) at 0.0154 s. These samples were visualized as the darkest regions in the T2 map, reflecting their superior transverse relaxation efficiency. In contrast, unmodified Fe_3O_4@MSN-NH_2 at both concentrations (ROI 3: 0.0688 s at 50 µg/mL; ROI 7: 0.0901 s at 5 µg/mL) exhibited significantly longer T2 values, indicating weaker contrast.

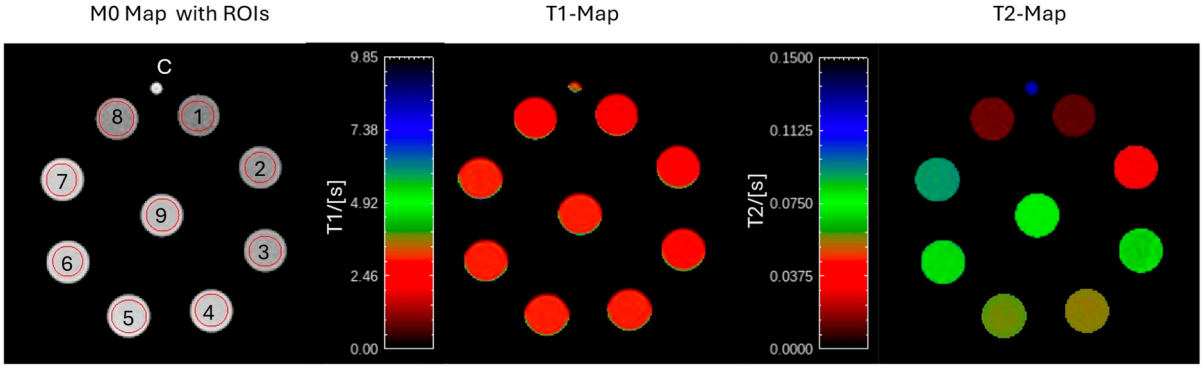

Figure 9. MRI relaxometry maps comparing M0, T1, T2 relaxation characterization of synthesized NPs. The M0 map exhibits regions of interest (ROIs 1–9) with control (C). The T1 map displays minor variation among samples (range: 0.00–9.85 s). In contrast, the T2 map shows major contrast differences, where Fe_3O_4@MSN-NH_2/FA (ROI 1) and Fe_3O_4@MSN-NH_2/FA/OXA (ROI 8) appear darkest, suggesting enhanced transverse relaxation efficiency.

At 5 µg/mL concentrations, Fe_3O_4@MSN-NH_2/FA (ROI 4) and Fe_3O_4@MSN-NH_2/FA/OXA (ROI 5) samples retained moderate contrast, while Fe_3O_4@MSN-NH_2/OXA (ROI 6) and Fe_3O_4@MSN-NH_2 (ROI 7) demonstrated poor performance.

The MRI studies verified that surface functionalization substantially impacts transverse relaxation efficiency. FA and OXA loading synergistically improved T2 contrast, likely resulting from slightly increased NP clustering and enhanced local magnetic inhomogeneities, which are key contributors known to intensify T2 relaxivity [85]. This effect was most apparent at higher concentrations (50 mg/mL), where Fe_3O_4@MSN–NH_2/FA and Fe_3O_4@MSN–NH_2/FA/OXA attained T2 values comparable to current clinical agents. These findings align with clinical iron oxide contrast agents such as Resovist, Ferumoxytol, and Ferumoxtran-10 (T_2 range: 0.008–0.030 s), positioning Fe_3O_4@MSN-NH_2/FA/OXA as a promising candidate for MRI-guided targeted chemotherapy. The strong T_2 contrast, combined with pH-responsive drug release and magnetic navigation, underscores the theranostic potential of this multi-functional platform.

The relatively consistent T1 values (~2.25–2.85 s) across all formulations suggest that longitudinal relaxation largely remained unaffected by surface modifications, while substantiating that these NPs primarily perform as T2 contrast agents.

3.4. Drug Loading Capacity

The concentration of Pt was quantified by ICP-OES to determine the OXA loading capacity in Fe_3O_4@MSN-NH_2/OXA, and Fe_3O_4@MSN-NH_2/FA/OXA using the commercial OXA as reference. To prepare samples for the analysis, the NPs were dissolved in 10 mL aqua regia and heated for 2 h. HPLCW was added to adjust the final volume to 50 mL, from which a 1 mL aliquot was taken for analysis. The results showed the Pt contents of Fe_3O_4@MSN-NH_2/OXA and Fe_3O_4@MSN-NH_2/FA/OXA were 5.07% and 14.60%, respectively. The drug loadings of Fe_3O_4@MSN-NH_2/OXA and Fe_3O_4@MSN-NH_2/FA/OXA were 10.33% and 29.73%, respectively (considering molecular weight of OXA is 397.29 g/mol). The FA-functionalized (Fe_3O_4@MSN-NH_2/FA/OXA) sample had a three-fold increase in OXA loading efficiency compared to the non-FA-functionalized (Fe_3O_4@MSN-NH_2/OXA) sample.

3.5. Drug Release with Magnetic Robot Actuated/Without Magnetic Robot

3.5.1. Overview of Release Profile and System Setup

The drug release profile was evaluated in previously explained the closed-loop perfusion system (Section 2.5, simulating physiological (pH 7.4) as well as tumor-mimicking (pH 5.0) environments, under controlled dynamic flow (~4.0 mls^{-1}) and MRP for site-specific NP accumulation (Figure 10a,b). The release was quantified by HPLC-UV (OXA was used as reference in HPLC-UV analysis), and the results are displayed in Figure 10c,d. The tubing dimensions (210.0 cm total length of the flow path with 5.0 mm inner diameter of plastic tubing and a 10.0 cm dialysis section with inner diameter of 7.00 mm) reflect engineering constraints, rather than physiological vessel sizes. Physiological relevance [86–88] and reproducibility were ensured through flow rate (Q) control at ~4.0 $mL{\cdot}s^{-1}$ (4.0×10^{-6} m^3/s), to produce laminar velocities and shear stresses comparable to microvascular ranges. The resulting Reynold number and flow regime were calculated as follows:

$$Re = \frac{\rho v D}{u} \quad (2)$$

where

Re = Reynold number (dimensionless)
ρ = fluid density (kg m^{-3}), (PBS: 1000 kg m^{-3} (25–37 °C))
v = average velocity (m s^{-1})
D = diameter of tubing (m)
u = dynamic viscosity (kg m^{-1} s^{-1})

Plastic tubing (D = 0.005 m)	$A \approx 1.96 \times 10^{-5}$ m^2, v = Q/A ≈ 0.204 m s^{-1}, Re = 1020
Dialysis section (D = 0.007 m)	$A \approx 3.85 \times 10^{-5}$ m^2, v = Q/A ≈ 0.104 m s^{-1}, Re = 728

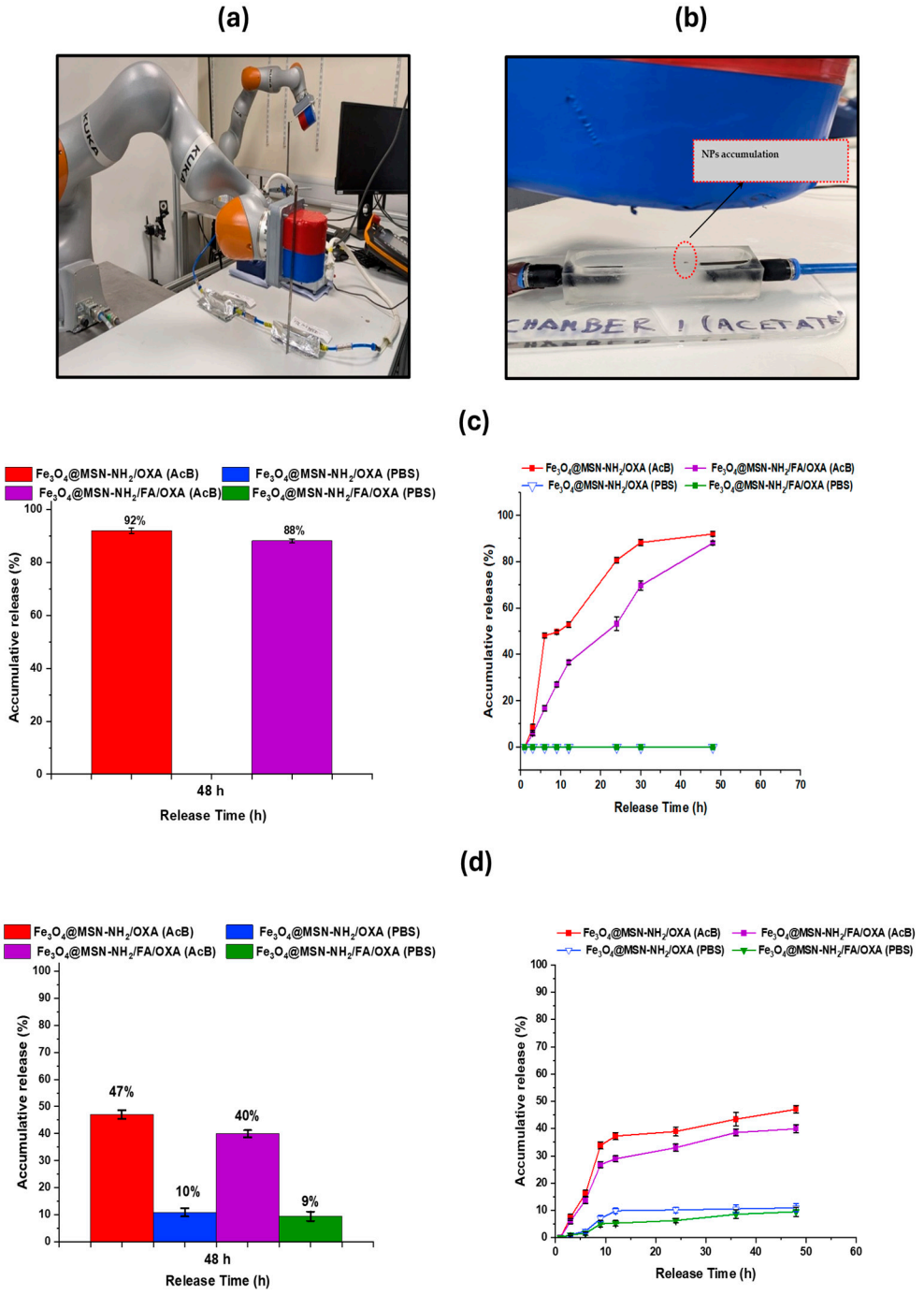

Figure 10. (**a**) MRP-controlled localization of Fe_3O_4@MSN-NH_2/FA/OXA in AcB and PBS flow system. (**b**) Accumulation of NPs by MRP. (**c**) MRP-assisted and (**d**) without MRP drug release test of Fe_3O_4@MSN-NH_2/OXA and Fe_3O_4@MSN-NH_2/FA/OXA in AcB and PBS in a dynamic flow system. Data are presented as percentage released standard error of the mean (SEM) from three independent experiments. In (**c**), the release data for both nano-formulations in PBS is reported as zero since it is below the detection limit.

The values of Reynolds number at 1020 (plastic tubing) and 728 (dialysis tubing) fall below the turbulence threshold of Re ≈ 2000 [89]. This confirms a stable laminar flow regime that minimizes shear-driven coating loss.

Although the Raynolds numbers are relatively high and comparative to large artery environments, wall shear stress is a more essential factor to consider in the dynamic flow setup, since it represents the frictional force per unit area imposed by fluid flowing along tubing. This could physically strip OXA molecules and coating from the surface, leading to a faster release rate than the static system. To calculate wall shear stress (t_w) [90], the following formula was used:

$$t_w = \frac{8uv}{D} \quad (3)$$

where

t_w = wall shear stress (Pa, N·m^{-2})

u = dynamic viscosity (Pa·s), (PBS at 25 °C = 0.001 Pa·s and at 37 °C = 0.0007 Pa·s)

v = average velocity (m·s^{-1})

D = diameter of tubing (m)

The wall shear stress values for plastic tubing were ~ 0.33 Pa (u = 0.001 Pa·s) and 0.23 Pa (u = 0.0007 Pa·s) and the values for dialysis tubing were 0.12 Pa (u = 0.001) and 0.08 Pa (u = 0.0007). These wall shear stress values align within microvascular/low shear conditions (0.1–1.5 Pa), making them representative of microvascular conditions [90].

3.5.2. MRP-Assisted Release Profiles

Under closed-loop dynamic perfusion system with MRP (Figure 10a), NPs gradually accumulated in the acidic chamber where the MRP was positioned, over a 48 h circulation period. Upon removal of the MRP from the acidic chamber (Figure 10b), the accumulated NPs were re-dispersed into the circulation system, indicating preserved superparamagnetic characteristics throughout the experiment. At physiological pH (7.4), both nano-formulations demonstrated OXA release below the detection limit over 48 h (Figure 10c), suggesting high OXA retention and colloidal stability throughout circulation. Under acidic conditions (pH 5.0), both samples exhibited significant pH-responsiveness release. Notably, Fe_3O_4@MSN-NH_2/OXA exhibited a faster initial release, reaching roughly 50% of OXA within 5 h and approximately 92% by 48 h. Conversely, Fe_3O_4@MSN-NH_2/FA/OXA demonstrated a more gradual release profile, reaching about 18% at 5 h and around 88% by the end of 48 h (Figure 10c).

3.5.3. Release Profiles Without MRP

In the absence of the MRP (Figure 10d), under the same dynamic perfusion condition, the release profiles of Fe_3O_4@MSN-NH_2/OXA and Fe_3O_4@MSN-NH_2/FA/OXA were controlled solely by pH-release conditions. Under physiological pH (7.4), both samples demonstrated minimal OXA release (<10%) over 48 h. At acidic (pH 5.0) environments, both samples exhibited more substantial OXA release, with approximately 47% for Fe_3O_4@MSN-NH_2/OXA and 40% Fe_3O_4@MSN-NH_2/FA/OXA. These findings verify the pH-responsiveness profiles of both samples and demonstrate the extra advantage of MRP-assisted navigation for controlled OXA release.

3.5.4. Mechanistic Interpretation

The drug release studies in the dynamic circulation system by MRP exhibited that both formulations (Fe_3O_4@MSN-NH_2/OXA and Fe_3O_4@MSN–NH_2/FA/OXA) have good stability under physiological environments (pH 7.4; chamber 1), which is important for preventing premature OXA leakage during systemic circulation. The low OXA release at pH 7.4 (<10% without MRP) verifies strong OXA–carrier interactions and stable colloidal profile. Under acidic conditions (AcB, pH 5.0), both samples demonstrated substantial OXA release, confirming their pH-responsive behavior. The faster OXA release observed for Fe_3O_4@MSN-NH_2/OXA is attributed to protonation of surface -NH_2 groups which reduces their interactions with OXA and enhances its diffusion from the mesoporous

structure. On the other hand, observed slower release for Fe_3O_4@MSN–NH_2/FA/OXA is likely attributed to steric hindrance and stronger binding interactions between the Pt center of OXA and electron-donating moieties in FA, as supported by XPS data.

3.5.5. Contribution of MRP Navigation

The MRP system exhibited spatially (site-specific accumulation) and temporally (extended, regulated release) controlled OXA release, enabling NPs' accumulation and sustained OXA diffusion over 48 h. The results showed that the application of MRP markedly improved OXA release under an acidic environment compared to without the MRP system. At pH 5.0, Fe_3O_4@MSN-NH_2/FA/OXA released ~88% under MRP control versus ~40% without MRP during 48 h (Figure 10c,d). This corresponds to more than a twofold enhancement in release efficiency attributable to MRP assistance. The enhancement reflects MRP-assisted NP accumulation in the acidic chamber, which maximized residence time and sustained OXA diffusion over the 48 h circulation period. While in the absence of MRP, OXA release kinetics were slower and had lower cumulative release, highlighting the critical role of MRP navigation in achieving controlled delivery under dynamic circulation conditions. Ultimately, this multi-responsive system offers a major advantage for enhancing drug accumulation at TME, while reducing the off-target exposure, highlighting the potential of these NPs for MRP-navigated cancer therapy.

3.5.6. Comparative Analysis with Literature

Table 6 compares drug loading, release profile, types of release, and targeting modality across multi-responsive Fe_3O_4 systems and selected pH-responsive Fe_3O_4-based nano-formulations reported in the literature, under dynamic circulation and static conditions. Although conventional static drug release studies, such as Tabasi et al. [53], achieved high release at pH 5.0 (>93%), the system was evaluated under static conditions without magnetic guidance or a dynamic circulation system, reducing its physiological relevance. Similarly, Moeni et al. [61] designed TPP-functionalized the Fe_3O_4@MSN–NH_2/OXA system for mitochondrial targeting, which displayed pH-responsive release of about 94%, but was also evaluated under static conditions, without dynamic perfusion or magnetic assistance. These constraints contrast with our system, which uniquely integrates closed-loop dynamic perfusion setup with MRP navigation and controlled drug release. Unlike conventional static pH-responsive systems, our formulations (Fe_3O_4@MSN–NH_2/OXA and Fe_3O_4@MSN–NH_2/FA/OXA) combine dynamic circulation with magnetically navigated MRP, enabling NP site-specific accumulation and controlled release. This system demonstrated no premature OXA release at simulated physiological pH 7.4 and more-than-twofold-higher release efficiency under tumor-simulated conditions (pH 5.0) compared to dynamic perfusion with no MRP.

Table 6. Comparison of drug loading, release profile, types of release, and targeting modality for Fe_3O_4-based nano-formulations under dynamic circulation and static conditions.

Formulations	Payload	Loading Metric and (Quantification Method)	Release Profile (48 h)	Type of Release Study	Targeting Modality	Ref.
Fe_3O_4@MSN-NH_2/FA/OXA	OXA	DL: 29.73% (ICP-OES)	pH 5.0: 88.0%, pH 7.4: ~0.0% (MRP) pH 5.0: ~40.0%, pH 7.4: <10.0% (no MRP)	Dynamic circulation ± MRP	FA-FOLR1 (active) + MRP	This study
Fe_3O_4@MSN-NH_2/OXA	OXA	DL: 10.33% (ICP-OES)	pH 5.0: ~94.0% (MRP), pH 7.4: ~0.0% (MRP) pH 5.0: ~47.0%, pH 7.4: <10.0% (no MRP)	Dynamic circulation/flow ± MRP	NH_2 surface + MRP	This study

Table 6. *Cont.*

Formulations	Payload	Loading Metric and (Quantification Method)	Release Profile (48 h)	Type of Release Study	Targeting Modality	Ref.
Fe_3O_4@MSN-NH_2/TPP/OXA	OXA	DL: 16.29% (ICP-OES)	pH 5.0: ~94.3% pH 7.4: 9.0%	Static-no flow	TPP mitochondrial targeting	[61]
Fe_3O_4@MSN-NH_2/OXA	OXA	DL: 10.33% (ICP-OES)	pH 5.0: ~88.4% pH 7.4: <10.0%	Static-no flow	NH_2 surface	[61]
Fe_3O_4@MSN/OXA	OXA	EE: 18.50% (ICP-OES)	pH 5.0: >93.0% pH 7.4: <10.0%	Static-no flow	Unmodified MSN	[53]
Fe_3O_4@MSN-NH_2/OXA	OXA	EE: 55.00% (ICP-OES)	pH 5: >93.0% pH 7.4: <10.0%	Static-no flow	NH_2 surface	[53]

Drug loading (DL); encapsulation efficiency (EE).

3.6. Proof of Principle of Targeted Cytotoxicity In Vitro

3.6.1. FOLR1 Gene Expression in Colorectal Cancer Cell Lines

We tested a panel of human colorectal cancer cell lines (Caco2, SW620, T84 and SW48 cells) for FOLR1 gene expression (FOLR1-positive) using RT-qPCR (Figure 11). All four cell lines demonstrated detectable levels of FOLR1 expression. Among them, Caco2 displayed the highest FOLR1 expression ($FOLR1^{high}$ or FOLR1-positive), while SW48 cells exhibited the lowest FOLR1 expression ($FOLR1^{low}$ or FOLR1-negative). Based on these results, Caco2 and SW48 were selected for further NP testing to represent FOLR1-positive and FOLR1-negative.

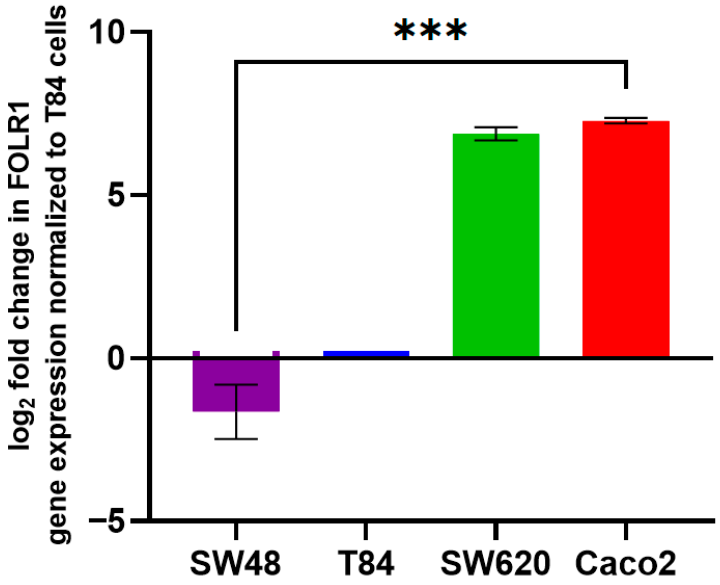

Figure 11. FOLR1 gene expression in human colorectal cancer cell lines (Caco2, SW620, T84 and SW48) determined by RT-qPCR. GAPDH served as the house-keeping gene; T84 cells were used as reference. Data are presented as $\log_2$ fold-change in FOLR1 gene expression normalized to T84 cells, expressed as mean ± standard error of the mean (SEM) for three independent replicates; *** denotes $p < 0.001$ (student *t*-test).

In gene expression studies, the detected variability in FOLR1 expression among colorectal cancer cell lines (Caco2, SW620, T84 and SW48) validates the rationale for choosing FA-functionalized NPs for targeted OXA delivery. Caco2 cells with $FOLR1^{high}$ expression provide a suitable model for evaluating receptor-mediated uptake, whereas SW48 cells serve as $FOLR1^{low}$ expression control. These data were comparable to that of the publicly available database, The Human Protein Atlas [91], which reports high FOLR1 gene expression in Caco2 cells and undetected levels in SW48 cells. The Human Protein

Atlas [91] confirms that the protein-level expression of FOLR1 in Caco2 and SW48 cells follows the same trend as gene expression results [57]. These distinct expression patterns establish a foundation for investigating whether FA conjugation improves NPs' specificity and cytotoxicity in FOLR1-positive cells, which is a critical step toward verifying targeted therapeutic potential.

3.6.2. Cytotoxicity of Functionalized Nanoparticles

We then tested the cytotoxicity of Fe_3O_4@MSN-NH_2, Fe_3O_4@MSN-NH_2/OXA, Fe_3O_4@MSN-NH_2/FA, and Fe_3O_4@MSN-NH_2/FA/OXA in FOLR1^{high} Caco2 and FOLR1^{low} SW48 cell lines. Fe_3O_4@MSN-NH_2 (Figure 12a) treatment on both cell lines showed a similar trend, but toxicity was observed at higher concentrations, due to the Fenton reaction [92–94]. However, FA-conjugated (Fe_3O_4@MSN-NH_2/FA) NPs showed not much toxicity with FOLR1^{low} SW48 cells (Figure 12c, $p < 0.0001$), while significantly greater cytotoxicity towards FOLR1^{high} Caco2 cells. To establish baseline OXA sensitivity, both cell lines were exposed to pure OXA (SW48 cells were markedly more sensitive to OXA than Caco2 cells) ($p < 0.0001$), and results are presented in Supplementary Information Figure S2. In Fe_3O_4@MSN-NH_2/OXA (Figure 12b), both Caco2 and SW48 cells displayed dose-dependent growth, with no distinct selectivity between the two cell lines. Also, Fe_3O_4@MSN-NH_2/FA/OXA (Figure 12d) inhibited proliferation in Caco2 and SW48 cell lines in a dose-responsive manner; however they had similar responses, suggesting that OXA sensitivity outweighed the contribution of FA-mediated uptake. The IC_{50} values for Fe_3O_4@MSN-NH_2, Fe_3O_4@MSN-NH_2/OXA, Fe_3O_4@MSN-NH_2/FA, and Fe_3O_4@MSN-NH_2/FA/OXA are presented in Table S5.

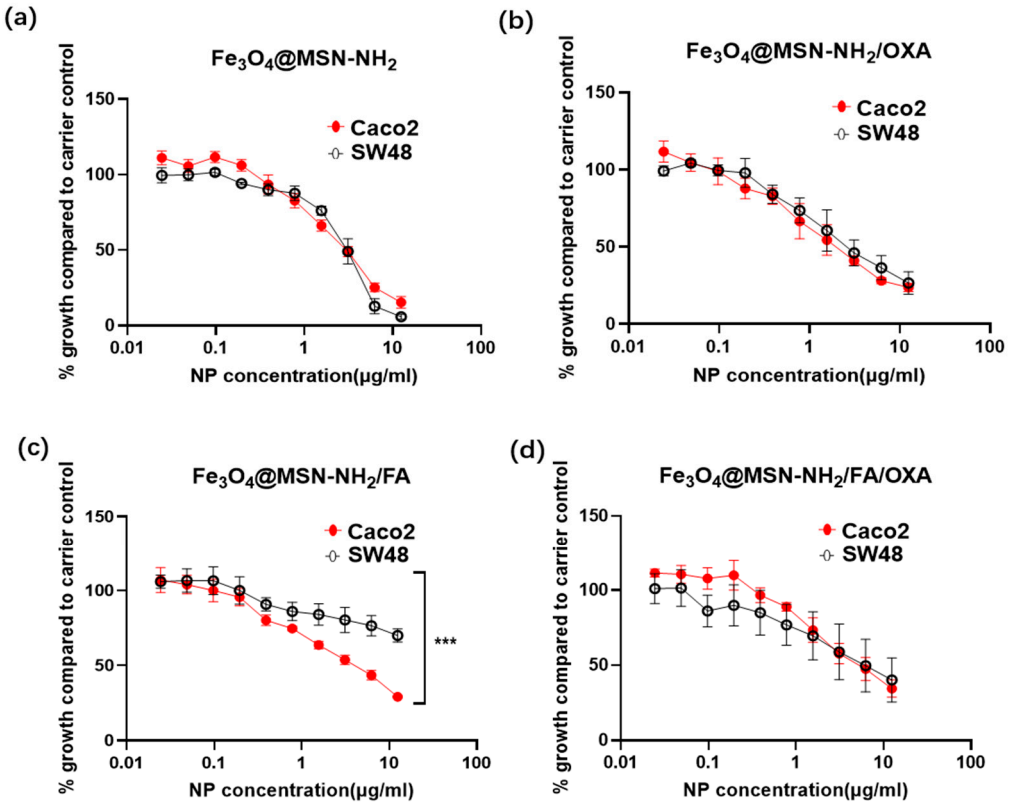

Figure 12. (**a**–**d**) Cytotoxicity of Fe_3O_4@MSN-NH_2 (**a**), Fe_3O_4@MSN-NH_2/OXA (**b**), Fe_3O_4@MSN-NH_2/FA (**c**), or Fe_3O_4@MSN-NH_2/FA/OXA. (**d**) NPs in FOLR1^{high} Caco2 cells and FOLR1^{low} SW48 cells assessed by MTT assay. Cell viability is expressed as mean percentage relative to carrier control-treated cells. Data are presented as mean ± standard error of the mean (SEM) (n = 3); *** $p < 0.001$ (two-way ANOVA).

The high cytotoxicity of FA-conjugated NPs in FOLR1^{High} Caco2 cells verifies that FA conjugation enhances receptor-mediated targeting (Figure 12c). The data validates the hypothesis that folate receptor expression affects NPs uptake and therapeutic response. However, in Fe_3O_4@MSN-NH_2/OXA and Fe_3O_4@MSN-NH_2/FA/OXA samples (Figures 12b and 12d, respectively), Caco2 and SW48 displayed very identical dose-dependent curves; hence, any FA-sensitive selectivity is not evident in OXA-loaded formulations. In combination with the differences in OXA loading (Section 3.4) between Fe_3O_4@MSN-NH_2/OXA and Fe_3O_4@MSN-NH_2/FA/OXA, these results highlight the requirement for further studies, particularly on alternative colorectal cancer cells that demonstrate differential FOLR1 gene expression levels but comparable OXA sensitivity.

It should be noted that Fe_3O_4-based drug delivery systems are known to accumulate in reticuloendothelial system (RES) organs and undergo gradual degradation [43], thereby necessitating comprehensive future studies on biodistribution, clearance, and long-term safety prior to clinical advancement.

Importantly, our MRP system is strategically intended to minimize off-target RES accumulation by actively navigating and controlling superparamagnetic nanocarriers at the tumor site. This strategy mitigates the natural tendency of NPs to localize in the liver and spleen, thereby improving their translation safety profile. Future work will focus on the comprehensive evaluation of OXA-loaded samples (Fe_3O_4@MSN-NH_2/OXA and Fe_3O_4@MSN-NH_2/FA/OXA) under MRP-assisted navigation, and magnetically induced hyperthermia performance under dynamic circulation platform, which will be reported in a forthcoming publication.

4. Conclusions

This study presents a novel approach for spatially and temporally controlled release of OXA using an MRP. The system employs Fe_3O_4@MSN-NH_2/OXA and Fe_3O_4@MSN-NH_2/FA/OXA nanoparticles. Extensive characterizations (FT-IR, XRD, XPS, LUMiSizer, DLS, zeta potential, VSM, and BET) confirmed successful fabrication, sequential surface functionalization, and mesoporous structure. All samples maintained their superparamagnetic characteristics. Compared to the Fe_3O_4@MSN-NH_2/OXA sample, FA-conjugated NPs (Fe_3O_4@MSN-NH_2/FA/OXA) exhibited excellent colloidal stability, strong T2-weighted contrast, and a three-fold-higher OXA loading efficiency (up to 29.7%), showing the advantages of FA conjugation. Additionally, HPLC-UV analysis confirmed MRP-controlled release with minimal/no premature leakage and improved site-specific delivery, which yields substantially higher drug release compared to a non-MRP-controlled system, ensuring sustained, pH-responsive release.

Building on this proof-of-concept work in a simulated TME, cytotoxicity assays on colorectal cancer cell lines with differential FOLR1 expression exhibited FOLR1-associated selectivity of FA-conjugated NPs, supporting receptor-mediated cellular uptake. To our knowledge, this is the first report to combine FA-conjugated Fe_3O_4@MSN-NH_2 NPs with an MRP for controlled release of OXA under physiologically relevant dynamic circulation/flow systems. This integrated strategy introduces a novel avenue for the design of MRP-navigated, ligand-targeted theranostic nanomedicines.

These initial biological evaluations support the platform's therapeutic potential and represent a significant advance toward further in vitro and in vivo validation. As the next step, we propose studies in tumor-bearing models under MRP navigation to evaluate therapeutic efficacy and translational potential. In summary, this work lays the foundational framework for the development of magnetically navigated, targeted chemotherapeutic drug delivery systems with potential applications in precision oncology.

Supplementary Materials: The supporting information can be downloaded at https://www.mdpi.com/article/10.3390/pr14040597/s1; Video S1: MRP-controlled drug release in simulated tumor condition; Video S2: MRP-guided drug flow in physiological conditions and Supplementary Information; Table S1: Summary of chemicals, quantities, experimental conditions, and post-reaction rinsing stages for the synthesis of nanoparticles; Table S2: Summary of information for magnetic robot platform setup (MRP) and dynamic circulation/flow system parameters; Table S3: The amount of mass loss at different temperature for Fe_3O_4@CTAB-SiO_2 and Fe_3O_4@MSN-NH_2 by TGA; Table S4: Mathematical values and fitting parameters used to generate the frequency dependent blocking temperature graph for Fe_3O_4, Fe_3O_4@CTAB-SiO_2, Fe_3O_4@CTAB-SiO_2-NH_2, and Fe_3O_4@MSN-NH_2; Table S5: The IC50 values for Fe_3O_4@MSN-NH_2, Fe_3O_4@MSN-NH_2/OXA, Fe_3O_4@MSN-NH_2/FA, and Fe_3O_4@MSN-NH_2/FA/OXA in SW48 cells and $CaCo_2$ cells; Figure S1: Temperature-dependent AC magnetic susceptibility showing ACX″ versus temperature for (a) Fe_3O_4, (b) Fe_3O_4@CTAB-SiO_2, (c) Fe_3O_4@CTAB-SiO_2-NH_2 and (d) Fe_3O_4@MSN-NH_2; Figure S2: Cytotoxicity of Oxaliplatin in $FOLR1^{high}$ $CaCo_2$ cells and $FOLR1^{low}$ SW48 cells assessed by MTT assay. Cell viability is expressed as mean percentage relative to carrier control-treated cells. Data are presented as mean ± standard error of the mean (SEM) (n = 3). *** $p < 0.001$ (two-way ANOVA).

Author Contributions: Conceptualization, M.M. and A.H.; methodology, M.M., M.E., R.M. and A.H.; formal analysis, M.M., M.R., O.C., Z.A., A.B. (Andrew Britton) and M.V.; investigation, M.M., H.S., M.R., Z.A. and M.V.; data curation, A.B. (Alistair Bacchetti); writing—original draft preparation, M.M.; writing—review and editing, M.M., M.E., A.B. (Alistair Bacchetti), J.D., H.S., M.R., O.C., Z.A., A.B. (Andrew Britton), J.E.S., L.K., P.V., R.M., M.V. and A.H.; visualization, Z.A.; supervision, M.V., R.M. and A.H.; All authors have read and agreed to the published version of the manuscript.

Funding: University of Leeds Sanctuary Scholarship and EPSRC grants (EP/P022464/1, EP/R00661X/1).

Data Availability Statement: Data and code are available upon reasonable request from the lead contact.

Acknowledgments: Masome Moeni would like to acknowledge the University of Leeds for the Sanctuary Scholarship and Alex Ferguson for his support. The authors would like to thank the School of Chemical and Process Engineering, University of Leeds, for the technical support, training and access to analytical equipment provided by Ben Douglas, Adrian Cunliffe and Simon Lloyd and Robert Harris and Barrington Hall. We would also like to thank Christopher Pask and Jeanine Williams from the School of Chemistry, University of Leed. We would like to extend sincere thanks to Elizabeth Willneff for her expert support and insightful contributions to the XPS analysis. We acknowledge support from the Henry Royce Institute, which funded the Versatile X-ray Spectroscopy Facility (VXSF) Facilities within the Bragg Center for Materials Research at Leeds.

Conflicts of Interest: The authors declare no conflicts of interest.

Abbreviations

The following abbreviations are used in this manuscript:

AcB	Acetate buffer
APTES	3-aminopropyltriethoxysilane
ACX″	Imaginary component of AC susceptibility
ATR	Attenuated total reflection
BET	Brunauer–Emmett–Teller
T_b	Blocking temperature
Caco2	Cancer Coli, colon cancer
CDR	Controlled drug release
CTAB	Cetyltrimethylammonium bromide
DAD	Diode array detector
DH	Hydrodynamic size
DL	Drug release

DLS	Dynamic light scattering
DMSO	Dimethyl sulfoxide
DOX	Doxorubicin
DTG	Derivative thermogravimetry
EDCI	1-ethyl-3-(3-dimethylaminopropyl) carbodiimide
EDX	Energy dispersive x-ray spectroscopy
EE	Encapsulation efficiency
EPM	Electro-permanent magnetic
EtOH	Ethanol
FA	Folic acid
FCS	Fetal calf serum
$FOLR1^{high}$	Folate receptor alpha high
$FOLR1^{low}$	Folate receptor alpha low
FR	Folate receptors
FT-IR	Fourier transfer inferred spectroscopy
FWHM	Full width at half maximum
HAADF	High annular dark-field imaging
HPLCW	HPLC grade water
HPLC-UV	High-performance liquid chromatography with ultraviolet detection
HR-TEM	High-resolution transmission electron microscopy
ICP-OES	inductively coupled plasma optical emission spectrometer
MRP	Magnetic robot actuated platform
MNP	Magnetic nanoparticle
MRI	Magnetic resonance imaging
MSN	Mesoporous silica nanoparticles
NH_2	Amine groups
NH_4NO_3	Ammonium nitrate
NHS	N-hydroxysuccinimide
NMP	N-Methyl-2-pyrrolidone
NPs	Nanoparticles
OXA	Oxaliplatin
PBS	Phosphate-buffered solution
Pt	Platinum
PXRD	Powder X-ray diffraction
RES	Reticuloendothelial system
ROI	Region-of-interest
RT-qPCR	Reverse Transcription Quantitative Polymerase Chain Reaction
RT	Retention time
S	Section
SAED	Selected area diffraction pattern
SI	Supplementary Information
SiO_2	Silicon dioxide
SQID-VSM	Superconducting quantum interference device vibrating sample magnetometer
T	Tesla
TDD	Targeted drug delivery
TEOS	Tetraethyl orthosilicate
TGA/DSC	Thermogravimetric and differential scanning calorimetry
TME	Tumor microenvironment
TFA	Trifluoracetic acid
WET	WET colloidal suspension
XPS	X-ray photoelectron spectroscopy
UHV	Ultra-high Vacuum
ZP	Zeta potential

References

1. Yu, C.; Wang, Z.; Sun, Z.; Zhang, L.; Zhang, W.; Xu, Y.; Zhang, J.J. Platinum-based combination therapy: Molecular rationale, current clinical uses, and future perspectives. *J. Med. Chem.* **2020**, *63*, 13397–13412. [CrossRef]
2. Anand, U.; Dey, A.; Singh Chandel, A.K.; Sanyal, R.; Mishra, A.; Pandey, D.K.; De Falco, V.; Upadhyay, A.P.; Kandimalla, R.; Chaudhary, A.; et al. Cancer chemotherapy and beyond: Current status, drug candidates, associated risks and progress in targeted therapeutics. *Genes Dis.* **2022**, *10*, 1367–1401. [CrossRef]
3. Rothenberg, M.L.; Oza, A.M.; Bigelow, R.H.; Berlin, J.D.; Marshall, J.L.; Ramanathan, R.K.; Hart, L.L.; Gupta, S.; Garay, C.A.; Burger, B.; et al. Superiority of oxaliplatin and fluorouracil-leucovorin compared with either therapy alone in patients with progressive colorectal cancer after irinotecan and fluorouracil-leucovorin: Interim results of a phase III trial. *J. Clin. Oncol. Off. J. Am. Soc. Clin. Oncol.* **2003**, *21*, 2059–2069. [CrossRef]
4. Alcindor, T.; Beauger, N. Oxaliplatin: A review in the era of molecularly targeted therapy. *Curr. Oncol.* **2011**, *18*, 18–25. [CrossRef]
5. Yothers, G.; O'connell, M.J.; Allegra, C.J.; Kuebler, J.P.; Colangelo, L.H.; Petrelli, N.J.; Wolmark, N. Oxaliplatin as adjuvant therapy for colon cancer: Updated results of NSABP C-07 trial, including survival and subset analyses. *J. Clin. Oncol.* **2011**, *29*, 3768–3774. [CrossRef]
6. Mauri, G.; Gori, V.; Bonazzina, E.; Amatu, A.; Tosi, F.; Bencardino, K.; Ruggieri, L.; Patelli, G.; Arena, S.; Bardelli, A.; et al. Oxaliplatin retreatment in metastatic colorectal cancer: Systematic review and future research opportunities. *Cancer Treat. Rev.* **2020**, *91*, 102112. [CrossRef]
7. Grolleau, F.; Gamelin, L.; Boisdron-Celle, M.; Lapied, B.; Pelhate, M.; Gamelin, E.C. A possible explanation for a neurotoxic effect of the anticancer agent oxaliplatin on neuronal voltage-gated sodium channels. *J. Neurophysiol.* **2001**, *85*, 2293–2297. [CrossRef]
8. Webster, R.G.; Brain, K.L.; Wilson, R.H.; Grem, J.L.; Vincent, A. Oxaliplatin induces hyperexcitability at motor and autonomic neuromuscular junctions through effects on voltage-gated sodium channels. *Br. J. Pharmacol.* **2005**, *146*, 1027–1039. [CrossRef]
9. Han, C.H.; Khwaounjoo, P.; Hill, A.G.; Miskelly, G.M.; McKeage, M.J. Predicting effects on oxaliplatin clearance: In vitro, kinetic and clinical studies of calcium- and magnesium-mediated oxaliplatin degradation. *Sci. Rep.* **2017**, *7*, 4073. [CrossRef]
10. Gan, L.; Liu, Z.; Sun, C. Obesity linking to hepatocellular carcinoma: A global view. *Biochim. Biophys. Acta (BBA) Rev. Cancer* **2018**, *1869*, 97–102. [CrossRef]
11. Wu, Y.; Liang, Y.; Liu, Y.D.; Hao, Y.; Tao, N.; Li, J.; Sun, X.; Zhou, M.; Liu, Y. A Bi_2S_3-embedded gellan gum hydrogel for localized tumor photothermal/antiangiogenic therapy. *J. Mater. Chem. B* **2021**, *9*, 3224–3234. [CrossRef] [PubMed]
12. Zafar, H.; Raza, F.; Ma, S.; Wei, Y.; Zhang, J.; Shen, Q. Recent progress on nanomedicine-induced ferroptosis for cancer therapy. *Biomater. Sci.* **2021**, *9*, 5092–5115. [CrossRef]
13. Sun, Q.; Zhou, Z.; Qiu, N.; Shen, Y. Rational Design of Cancer Nanomedicine: Nanoproperty Integration and Synchronization. *Adv. Mater.* **2017**, *29*, 1606628. [CrossRef]
14. Feng, C.; Wang, Y.; Xu, J.; Zheng, Y.; Zhou, W.; Wang, Y.; Luo, C. Precisely Tailoring Molecular Structure of Doxorubicin Prodrugs to Enable Stable Nanoassembly, Rapid Activation, and Potent Antitumor Effect. *Pharmaceutics* **2024**, *16*, 1582. [CrossRef]
15. Wang, Y.; Xu, Y.; Song, J.; Liu, X.; Liu, S.; Yang, N.; Wang, L.; Liu, Y.; Zhao, Y.; Zhou, W.; et al. Tumor Cell-Targeting and Tumor Microenvironment–Responsive Nanoplatforms for the Multimodal Imaging-Guided Photodynamic/Photothermal/Chemodynamic Treatment of Cervical Cancer. *Int. J. Nanomed.* **2024**, *19*, 5837–5858. [CrossRef]
16. Yuan, H.; Chen, Y.; Hu, Y.; Li, Y.; Zhang, H.; Zhang, S.; Chen, Q.; Zhou, W.; Sun, J.; He, Z.; et al. Disulfide bond-driven nanoassembly of lipophilic epirubicin prodrugs for breast cancer therapy. *J. Pharm. Investig.* **2025**, *55*, 889–902. [CrossRef]
17. Dadfar, S.M.; Roemhild, K.; Drude, N.I.; von Stillfried, S.; Knüchel, R.; Kiessling, F.; Lammers, T. Iron oxide nanoparticles: Diagnostic, therapeutic and theranostic applications. *Adv. Drug Deliv. Rev.* **2019**, *138*, 302–325. [CrossRef]
18. Zhao, J.; Li, X.; Wang, X.; Wang, X. Fabrication of Hybrid Nanostructures Based on Fe_3O_4 Nanoclusters as Theranostic Agents for Magnetic Resonance Imaging and Drug Delivery. *Nanoscale Res. Lett.* **2019**, *14*, 200. [CrossRef] [PubMed]
19. Mahmoudi, R.; Esmaeili, A.; Nematollahzadeh, A. Preparation of Fe_3O_4/Au/Ag_3VO_4 nanocomposite coated with Caerophyllum macropodum extract modified with oleic acid for theranostics agent in medical imaging. *J. Photochem. Photobiol. A Chem.* **2021**, *425*, 113724. [CrossRef]
20. Divband, B.; Gharehaghaji, N.; Hassani, S. Fe_3O_4/Graphene-Based Nanotheranostics for Bimodal Magnetic Resonance/Fluorescence Imaging and Cancer Therapy. *J. Inorg. Organomet. Polym. Mater.* **2022**, *32*, 4443–4460. [CrossRef]
21. Shen, Z.; Liu, T.; Li, Y.; Lau, J.; Yang, Z.; Fan, W.; Zhou, Z.; Shi, C.; Ke, C.; Bregadze, V.I.; et al. Fenton-Reaction-Acceleratable Magnetic Nanoparticles for Ferroptosis Therapy of Orthotopic Brain Tumors. *ACS Nano* **2018**, *12*, 11355–11365. [CrossRef]
22. Maeda, H. Tumor-selective delivery of macromolecular drugs via the EPR effect: Background and future prospects. *Bioconjugate Chem.* **2010**, *21*, 797–802. [CrossRef]
23. Akhtar, M.J.; Ahamed, M.; Alhadlaq, H.A.; Alrokayan, S.A.; Kumar, S. Targeted anticancer therapy: Overexpressed receptors and nanotechnology. *Clin. Chim. Acta* **2014**, *436*, 78–92. [CrossRef]

24. Muhamad, N.; Plengsuriyakarn, T.; Na-Bangchang, K. Application of active targeting nanoparticle delivery system for chemotherapeutic drugs and traditional/herbal medicines in cancer therapy: A systematic review. *Int. J. Nanomed.* **2018**, *13*, 3921–3935. [CrossRef]
25. Nosrati, H.; Salehiabar, M.; Sefidi, N.; Javani, S.; Davaran, S.; Danafar, H. Target Delivery of Iron Oxide Magnetic Nanoparticles for Imaging and Treatment. In *Magnetic Nanoheterostructures: Diagnostic, Imaging and Treatment*; Sharma, S.K., Javed, Y., Eds.; Springer: Cham, Switzerland, 2020; pp. 267–285.
26. Yoo, J.; Park, C.; Yi, G.; Lee, D.; Koo, H. Active Targeting Strategies Using Biological Ligands for Nanoparticle Drug Delivery Systems. *Cancers* **2019**, *11*, 640. [CrossRef]
27. Salehnia, Z.; Shahbazi-Gahrouei, D.; Akbarzadeh, A.; Baradaran, B.; Farajnia, S.; Naghibi, M. Synthesis and characterisation of iron oxide nanoparticles conjugated with epidermal growth factor receptor (EGFR) monoclonal antibody as MRI contrast agent for cancer detection. *IET Nanobiotechnol.* **2019**, *13*, 400–406. [CrossRef]
28. Unnikrishnan, B.S.; Sen, A.; Preethi, G.U.; Joseph, M.M.; Maya, S.; Shiji, R.; Anusree, K.S.; Sreelekha, T.T. Folic acid-appended galactoxyloglucan-capped iron oxide nanoparticles as a biocompatible nanotheranostic agent for tumor-targeted delivery of doxorubicin. *Int. J. Biol. Macromol.* **2020**, *168*, 130–142. [CrossRef]
29. Sanchez, C.; El Hajj Diab, D.; Connord, V.; Clerc, P.; Meunier, E.; Pipy, B.; Payre, B.; Tan, R.P.; Gougeon, M.; Carrey, J.; et al. Targeting a G-protein-coupled receptor overexpressed in endocrine tumors by magnetic nanoparticles to induce cell death. *ACS Nano* **2014**, *8*, 1350–1363. [CrossRef]
30. Pineux, F.; Federico, S.; Klotz, K.-N.; Kachler, S.; Michiels, C.; Sturlese, M.; Prato, M.; Spalluto, G.; Moro, S.; Bonifazi, D. Targeting G Protein-Coupled Receptors with Magnetic Carbon Nanotubes: The Case of the A3 Adenosine Receptor. *ChemMedChem* **2020**, *15*, 1909–1920. [CrossRef]
31. Lopez, S.F.; Hallali, N.; Lalatonne, Y.; Hillion, A.; Antunes, J.C.; Serhan, N.; Clerc, P.; Fourmy, D.; Motte, L.; Carrey, J.; et al. Magneto-mechanical destruction of cancer-associated fibroblasts using ultra-small iron oxide nanoparticles and low frequency rotating magnetic fields. *Nanoscale Adv.* **2021**, *4*, 421–436. [CrossRef]
32. Gonzalez, T.; Muminovic, M.; Nano, O.; Vulfovich, M. Folate Receptor Alpha—A Novel Approach to Cancer Therapy. *Int. J. Mol. Sci.* **2024**, *25*, 1046. [CrossRef]
33. Elwood, P.C. Molecular cloning and characterization of the human folate-binding protein cDNA from placenta and malignant tissue culture (KB) cells. *J. Biol. Chem.* **1989**, *264*, 14893–14901. [CrossRef]
34. Zayed, A.L.; Bustami, R.T.; Alabsi, W.; El-Elimat, T. Development and Validation of a Rapid High-Performance Liquid Chromatography–Tandem Mass Spectrometric Method for Determination of Folic Acid in Human Plasma. *Pharmaceuticals* **2018**, *11*, 52. [CrossRef]
35. Cal, P.M.S.D.; Frade, R.F.M.; Chudasama, V.; Cordeiro, C.; Caddick, S.; Gois, P.M.P. Targeting cancer cells with folic acid-iminoboronate fluorescent conjugates. *Chem. Commun.* **2014**, *50*, 5261–5263. [CrossRef]
36. Slastnikova, T.A.; Rosenkranz, A.A.; Zalutsky, M.R.; Sobolev, A.S. Modular nanotransporters for targeted intracellular delivery of drugs: Folate receptors as potential targets. *Curr. Pharm. Des.* **2015**, *21*, 1227–1238. [CrossRef]
37. Shiji, R.; Joseph, M.M.; Anitha, S.D.C.; Pillai, K.R.; Unnikrishnan, B.S.; Sreelekha, T.T. Galactomannan armed superparamagnetic iron oxide nanoparticles as a folate receptor targeted multi-functional theranostic agent in the management of cancer. *Int. J. Biol. Macromol.* **2022**, *219*, 740–753. [CrossRef]
38. Berg, K.C.G.; Eide, P.W.; Eilertsen, I.A.; Johannessen, B.; Bruun, J.; Danielsen, S.A.; Bjørnslett, M.; Meza-Zepeda, L.A.; Eknæs, M.; Lind, G.E.; et al. Multi-omics of 34 colorectal cancer cell lines—A resource for biomedical studies. *Mol. Cancer* **2017**, *16*, 116. [CrossRef]
39. Veiseh, O.; Gunn, J.W.; Zhang, M. Design and fabrication of magnetic nanoparticles for targeted drug delivery and imaging. *Adv. Drug Deliv. Rev.* **2010**, *62*, 284–304. [CrossRef]
40. Samadi, M.; Shokrollahi, H.; Zamanian, A. The magnetic-field-assisted synthesis of the Co-ferrite nanoparticles via reverse co-precipitation and their magnetic and structural properties. *Mater. Chem. Phys.* **2018**, *215*, 355–359. [CrossRef]
41. Chen, Y.; Hou, S. Recent progress in the effect of magnetic iron oxide nanoparticles on cells and extracellular vesicles. *Cell Death Discov.* **2023**, *9*, 195. [CrossRef]
42. Mohammed, L.; Gomaa, H.; Ragab, D.M.; Zhu, J. Magnetic nanoparticles for environmental and biomedical applications: A review. *Particuology* **2017**, *30*, 1–14. [CrossRef]
43. Aram, E.; Moeni, M.; Abedizadeh, R.; Sabour, D.; Sadeghi-Abandansari, H.; Gardy, J.; Hassanpour, A. Smart and Multi-Functional Magnetic Nanoparticles for Cancer Treatment Applications: Clinical Challenges and Future Prospects. *Nanomaterials* **2022**, *12*, 3567. [CrossRef]
44. Gao, M.; Li, W.; Dong, J.; Zhang, Z.R.; Yang, B. Synthesis and Characterization of Superparamagnetic Fe_3O_4@SiO_2 Core-Shell Composite Nanoparticles. *World J. Condens. Matter Phys.* **2011**, *1*, 49–54. [CrossRef]

45. Cheng, J.; Tan, G.; Li, W.; Li, J.; Wang, Z.; Jin, Y.J.R.A. Preparation, characterization and in vitro photodynamic therapy of a pyropheophorbide-a-conjugated Fe_3O_4 multifunctional magnetofluorescence photosensitizer. *RSC Adv.* **2016**, *6*, 37610–37620. [CrossRef]
46. Cheng, J.; Tan, G.; Li, W.; Zhang, H.; Li, S.; Wang, Z.; Jin, Y. Preparation, Characterization, and Spectral Property Studies on Methotrexate Conjugated Multifunctional Fe_3O_4-Pyropheophorbide-a Fluorescence Nanoparticles. *J. Nanosci. Nanotechnol.* **2017**, *17*, 4461–4470.
47. Sobhanardakani, S.; Jafari, A.; Zandipak, R.; Meidanchi, A. Removal of heavy metal (Hg(II) and Cr(VI)) ions from aqueous solutions using Fe_2O_3@SiO_2 thin films as a novel adsorbent. *Process Saf. Environ. Prot.* **2018**, *120*, 348–357. [CrossRef]
48. Lerma, T.A.; Garcés, V.; Palencia, M. Novel multi- and bio-functional hybrid polymer hydrogels based on bentonite-poly(acrylic acid) composites and sorbitol polyesters: Structural and functional characterization. *Eur. Polym. J.* **2020**, *128*, 109627.
49. Chaurasia, A.K.; Thorat, N.D.; Tandon, A.; Kim, J.-H.; Park, S.H.; Kim, K.K. Coupling of radiofrequency with magnetic nanoparticles treatment as an alternative physical antibacterial strategy against multiple drug resistant bacteria. *Sci. Rep.* **2016**, *6*, 33662. [CrossRef]
50. Chen, Y.; Li, J.; Yuan, Z.; Feng, J.; Chen, Z. Metabolic fate and subchronic biological effects of core–shell structured Fe_3O_4@SiO_2-NH_2 nanoparticles. *Nanotoxicology* **2018**, *12*, 621–636.
51. Fang, Z.; Li, X.; Xu, Z.; Du, F.; Wang, W.; Shi, R.; Gao, D. Hyaluronic acid-modified mesoporous silica-coated superparamagnetic Fe_3O_4 nanoparticles for targeted drug delivery. *Int. J. Nanomed.* **2019**, *14*, 5785–5797. [CrossRef]
52. Camacho-Fernández, J.C.; González-Quijano, G.K.; Séverac, C.; Dague, E.; Gigoux, V.; Santoyo-Salazar, J.; Martinez-Rivas, A. Nanobiomechanical behavior of Fe_3O_4@SiO_2 and Fe_3O_4@SiO_2–NH_2 nanoparticles over HeLa cells interfaces. *Nanotechnology* **2021**, *32*, 385702. [CrossRef]
53. Tabasi, H.; Mosavian, M.T.H.; Sabouri, Z.; Khazaei, M.; Darroudi, M. pH-responsive and CD44-targeting by Fe_3O_4/MSNs-NH_2 nanocarriers for Oxaliplatin loading and colon cancer treatment. *Inorg. Chem. Commun.* **2021**, *125*, 108430. [CrossRef]
54. Tabasi, H.; Mosavian, M.T.H.; Darroudi, M.; Khazaei, M.; Hashemzadeh, A.; Sabouri, Z. Synthesis and characterization of amine-functionalized Fe_3O_4/Mesoporous Silica Nanoparticles (MSNs) as potential nanocarriers in drug delivery systems. *J. Porous Mater.* **2022**, *29*, 1817–1828. [CrossRef]
55. Hussain, A.; Hussain, M.; Alam, M.S.; Yasir, M.; Mohammad Khan, S.; Ud Din, S.; Hussain, N.; Hussain, E. Biogenic PAG-FeNPs from Prunus armeniaca (Gum) as robust colorimetric sensors for methyl orange detection. *Results Chem.* **2024**, *11*, 101789. [CrossRef]
56. Ciuti, G.; Donlin, R.; Valdastri, P.; Arezzo, A.; Menciassi, A.; Morino, M.; Dario, P. Robotic versus manual control in magnetic steering of an endoscopic capsule. *Endoscopy* **2009**, *42*, 148–152. [CrossRef]
57. Koleoso, M.; Feng, X.; Xue, Y.; Li, Q.; Munshi, T.; Chen, X. Micro/nanoscale magnetic robots for biomedical applications. *Mater. Today Bio* **2020**, *8*, 100085. [CrossRef]
58. Dupont, P.E.; Nelson, B.J.; Goldfarb, M.; Hannaford, B.; Menciassi, A.; O'Malley, M.K.; Simaan, N.; Valdastri, P.; Yang, G.-Z. A decade retrospective of medical robotics research from 2010 to 2020. *Sci. Robot.* **2021**, *6*, eabi8017. [CrossRef]
59. Yang, Z.; Zhang, L. Magnetic Actuation Systems for Miniature Robots: A Review. *Adv. Intell. Syst.* **2020**, *2*, 2000082. [CrossRef]
60. Moeni, M.; Edokali, M.; Rogers, M.; Cespedes, O.; Tliba, L.; Habib, T.; Menzel, R.; Hassanpour, A. Effect of reaction and post-treatment conditions on physico-chemical properties of magnetic iron oxide nano-particles. *Particuology* **2024**, *91*, 155–167. [CrossRef]
61. Moeni, M.; Edokali, M.; Rogers, M.; Cespedes, O.; Abedizadeh, R.; Khorasani, H.R.; Aram, E.; Sadeghi-Abandansari, H.; Gardy, J.; Sabour, D.; et al. Engineering Triphenyl Phosphonium Conjugated Iron Oxide Nanoparticles for Oxaliplatin loading: Application in Cancer Treatment. *Chem. Eng. Res. Des.* **2025**, *220*, 482–499. [CrossRef]
62. Ngo, M.T.; Lee, U.Y.; Ha, H.; Jin, N.; Chung, G.H.; Kwak, Y.-G.; Jung, J.; Kwak, H.S. Comparison of Hemodynamic Visualization in Cerebral Arteries: Can Magnetic Resonance Imaging Replace Computational Fluid Dynamics? *J. Pers. Med.* **2021**, *11*, 253. [CrossRef] [PubMed]
63. Yang, Y.; Guo, X.; Wei, K.; Wang, L.; Yang, D.; Lai, L.; Cheng, M.; Liu, Q. Synthesis and drug-loading properties of folic acid-modified superparamagnetic Fe_3O_4 hollow microsphere core/mesoporous SiO_2 shell composite particles. *J. Nanoparticle Res.* **2013**, *16*, 2210. [CrossRef]
64. Rana, S.; Shetake, N.G.; Barick, K.C.; Pandey, B.N.; Salunke, H.G.; Hassan, P.A. Folic acid conjugated Fe_3O_4 magnetic nanoparticles for targeted delivery of doxorubicin. *Dalton Trans.* **2016**, *45*, 17401–17408. [CrossRef]
65. Ni, Y.; Deng, P.; Yin, R.; Zhu, Z.; Ling, C.; Ma, M.; Wang, J.; Li, S.; Liu, R. Effect and mechanism of paclitaxel loaded on magnetic Fe_3O_4@mSiO_2-NH_2-FA nanocomposites to MCF-7 cells. *Drug Deliv.* **2022**, *30*, 64–82. [CrossRef]
66. Gong, Y.; Liu, G.; Wang, Q.; Zhu, A.; Liu, P.; Wu, Q. Synthesis of a novel mesoporous Fe_3O_4@SiO_2/CTAB-SiO_2 composite material and its application in the efficient removal of bisphenol A from water. *Colloid Polym. Sci.* **2021**, *299*, 807–822. [CrossRef]
67. Kim, Y.S.; An, G.S. Surface Engineering of Fe_3O_4@SiO_2 Core–Shell Nanoparticles: Role of CTAB/TEOS Ratio. *Ceram. Int.* **2024**, *51*, 379–385. [CrossRef]

68. Yang, Y.; Huang, M.; Qian, J.; Gao, D.; Liang, X. Tunable Fe_3O_4 Nanorods for Enhanced Magnetic Hyperthermia Performance. *Sci. Rep.* **2020**, *10*, 8331. [CrossRef]
69. Dawn, R.; Zzaman, M.; Faizal, F.; Kiran, C.; Kumari, A.; Shahid, R.; Panatarani, C.; Joni, I.M.; Verma, V.K.; Sahoo, S.; et al. Origin of Magnetization in Silica-coated Fe_3O_4 Nanoparticles Revealed by Soft X-ray Magnetic Circular Dichroism. *Braz. J. Phys.* **2022**, *52*, 99. [CrossRef]
70. Ulu, A.; Ozcan, I.; Koytepe, S.; Ateş, B. Design of epoxy-functionalized Fe_3O_4@MCM-41 core-shell nanoparticles for enzyme immobilization. *Int. J. Biol. Macromol.* **2018**, *115*, 1122–1130. [CrossRef] [PubMed]
71. Zhao, J.; Shu, Y.; Zhang, P. Solid-state CTAB-assisted synthesis of mesoporous Fe_3O_4 and Au@Fe_3O_4 by mechanochemistry. *Chin. J. Catal.* **2019**, *40*, 1078–1084. [CrossRef]
72. Jia, Y.-p.; Shi, K.; Liao, J.; Peng, J.; Hao, Y.; Qu, Y.; Chen, L.J.; Liu, L.; Yuan, X.; Qian, Z.; et al. Effects of Cetyltrimethylammonium Bromide on the Toxicity of Gold Nanorods Both In Vitro and In Vivo: Molecular Origin of Cytotoxicity and Inflammation. *Small Methods* **2020**, *4*, 1900799. [CrossRef]
73. Kim, K.-S.; Winograd, N.; Davis, R.E. Electron spectroscopy of platinum-oxygen surfaces and application to electrochemical studies. *J. Am. Chem. Soc.* **1971**, *93*, 6296–6297. [CrossRef]
74. Nefedov, V.I. X-ray photoelectron study of ligands in coordination compounds. *J. Mol. Struct.* **1978**, *46*, 251–268. [CrossRef]
75. Drawdy, J.E.; Hoflund, G.B.; Gardner, S.D.; Yngvadóttir, E.; Schryer, D.R. Effect of pretreatment on a platinized tin oxide catalyst used for low-temperature Co oxidation. *Surf. Interface Anal.* **1990**, *16*, 369–374. [CrossRef]
76. Mishra, S.; Manna, K.; Kayal, U.; Saha, M.; Chatterjee, S.; Chandra, D.; Hara, M.; Datta, S.; Bhaumik, A.; Das Saha, K. Folic acid-conjugated magnetic mesoporous silica nanoparticles loaded with quercetin: A theranostic approach for cancer management. *RSC Adv.* **2020**, *10*, 23148–23164. [CrossRef]
77. Pochapski, D.J.; Carvalho dos Santos, C.; Leite, G.W.; Pulcinelli, S.H.; Santilli, C.V. Zeta Potential and Colloidal Stability Predictions for Inorganic Nanoparticle Dispersions: Effects of Experimental Conditions and Electrokinetic Models on the Interpretation of Results. *Langmuir* **2021**, *37*, 13379–13389. [CrossRef]
78. Sadat, M.E.; Bud'ko, S.L.; Ewing, R.C.; Xu, H.; Pauletti, G.M.; Mast, D.B.; Shi, D. Effect of Dipole Interactions on Blocking Temperature and Relaxation Dynamics of Superparamagnetic Iron-Oxide (Fe_3O_4) Nanoparticle Systems. *Materials* **2023**, *16*, 496.
79. Noguchi, S.; Trisnanto, S.B.; Yamada, T.; Ota, S.; Takemura, Y. AC Magnetic Susceptibility of Magnetic Nanoparticles Measured Under DC Bias Magnetic Field. *J. Magn. Soc. Jpn.* **2022**, *46*, 42–48. [CrossRef]
80. Kushwaha, P.; Chauhan, P. Influence of different surfactants on morphological, structural, optical, and magnetic properties of α-Fe_2O_3 nanoparticles synthesized via co-precipitation method. *Appl. Phys. A* **2021**, *128*, 18.
81. Rajan, A.; Kaczmarek-Szczepańskac, B.; Sahu, N.K. Magneto-thermal response of Fe_3O_4@CTAB nanoparticles for cancer hyperthermia applications. *Mater. Today Commun.* **2021**, *28*, 102583. [CrossRef]
82. Meng, C.; Zhikun, W.; Qiang, L.; Chunling, L.; Shuangqing, S.; Songqing, H. Preparation of amino-functionalized Fe_3O_4@mSiO_2 core-shell magnetic nanoparticles and their application for aqueous Fe^{3+} removal. *J. Hazard. Mater.* **2018**, *341*, 198–206. [CrossRef]
83. Nguyen, M.D.; Tran, H.-V.; Xu, S.; Lee, T.R. Fe_3O_4 Nanoparticles: Structures, Synthesis, Magnetic Properties, Surface Functionalization, and Emerging Applications. *Appl. Sci.* **2021**, *11*, 11301. [CrossRef]
84. Goto, H.; Futagawa, M.; Takemura, Y.; Ota, S. Effects of Néel and Brownian relaxations on dynamic magnetization empirically characterized in single-core and multicore structures of magnetic nanoparticles. *Nanoscale* **2025**, *17*, 12817–12825. [CrossRef]
85. Simon, G.H.; Bauer, J.S.; Saborovski, O.; Fu, Y.; Corot, C.; Wendland, M.F.; Daldrup-Link, H.E. T1 and T2 relaxivity of intracellular and extracellular USPIO at 1.5T and 3T clinical MR scanning. *Eur. Radiol.* **2006**, *16*, 738–745.
86. Lindegaard, K.F.; Lundar, T.; Wiberg, J.; Sjøberg, D.I.K.; Aaslid, R.; Nornes, H. Variations in middle cerebral artery blood flow investigated with noninvasive transcranial blood velocity measurements. *Stroke* **1987**, *18*, 1025–1030. [CrossRef] [PubMed]
87. Pian, Q.; Alfadhel, M.A.H.; Tang, J.; Lee, G.V.; Li, B.; Fu, B.; Ayata, Y.; Yaseen, M.A.; Boas, D.A.; Secomb, T.W.; et al. Cortical microvascular blood flow velocity mapping by combining dynamic light scattering optical coherence tomography and two-photon microscopy. *J. Biomed. Opt.* **2023**, *28*, 076003. [CrossRef] [PubMed]
88. Contreras-Sánchez, H.A.; Zabel, W.J.; Flueraru, C.; Lilge, L.; Taylor, E.; Vitkin, A. Characterizing Normal and Tumour Blood Microcirculatory Systems Using Optical Coherence Tomography. *Photonics* **2024**, *11*, 891. [CrossRef]
89. Trịnh, K.T. On The Critical Reynolds Number For Transition From Laminar To Turbulent Flow. *arXiv* **2010**, arXiv:1007.0810. [CrossRef]
90. Papaioannou, T.G.; Stefanadis, C. Vascular wall shear stress: Basic principles and methods. *Hell. J. Cardiol.* **2005**, *46*, 9–15.
91. Uhlén, M.; Zhang, C.; Lee, S.; Sjöstedt, E.; Fagerberg, L.; Bidkhori, G.; Benfeitas, R.; Arif, M.; Liu, Z.; Edfors, F.; et al. A pathology atlas of the human cancer transcriptome. *Science* **2017**, *357*, eaan2507. [CrossRef] [PubMed]
92. Luo, C.; Li, X.; Yan, H.; Guo, Q.; Liu, J.; Li, Y. Iron oxide nanoparticles induce ferroptosis under mild oxidative stress in vitro. *Sci. Rep.* **2024**, *14*, 31383. [CrossRef] [PubMed]

93. Meng, Y.Q.; Shi, Y.N.; Zhu, Y.P.; Liu, Y.Q.; Gu, L.W.; Liu, D.D.; Ma, A.; Xia, F.; Guo, Q.; Xu, C.C.; et al. Recent trends in preparation and biomedical applications of iron oxide nanoparticles. *J. Nanobiotechnol.* **2024**, *22*, 24. [CrossRef] [PubMed]
94. Yadav, R.K.; Verma, S.; Ramakant, R.; Singh, A.K.; Pandey, V. Iron Oxide Nanoparticle Genotoxicity, ROS Production, and Epigenetic Alterations: A Comprehensive Review. *Int. J. For. Anim. Fish. Res.* **2025**, *9*, 1–16. [CrossRef]

Disclaimer/Publisher's Note: The statements, opinions and data contained in all publications are solely those of the individual author(s) and contributor(s) and not of MDPI and/or the editor(s). MDPI and/or the editor(s) disclaim responsibility for any injury to people or property resulting from any ideas, methods, instructions or products referred to in the content.